



# Dynamics of attached turbulent cavitating flows

Guoyu Wang<sup>a</sup>, Inanc Senocak<sup>b</sup>, Wei Shyy<sup>b,\*</sup>, Toshiaki Ikohagi<sup>c</sup>, Shuliang Cao<sup>d</sup>

<sup>a</sup>*School of Vehicle and Transportation Engineering, Beijing Institute of Technology, Beijing 100081, People's Republic of China*

<sup>b</sup>*Department of Aerospace Engineering, Mechanics and Engineering Science, University of Florida, 231 Aerospace Building,  
P.O. Box 116250, Gainesville, FL 32611, USA*

<sup>c</sup>*Institute of Fluid Science, Tohoku University, Sendai, 980-8577 Japan*

<sup>d</sup>*Department of Thermal Engineering, Tsinghua University, Beijing 100084, People's Republic of China*

---

## Abstract

Stationary and non-stationary characteristics of attached, turbulent cavitating flows around solid objects are reviewed. Different cavitation regimes, including incipient cavitation with traveling bubbles, sheet cavitation, cloud cavitation, and supercavitation, are addressed along with both visualization and quantitative information. Clustered hairpin type of counter-rotating vapor vortices at incipient cavitation, and finger-like structure in the leading edge and an oscillatory, wavy structure in the trailing edge with sheet cavitation are assessed. Phenomena such as large-scale vortex structure and rear re-entrant jet associated with cloud cavitation, and subsequent development in supercavitation are described. Experimental evidence indicates that the lift and drag coefficients are clearly affected by the cavitating flow structure, reaching minimum and maximum, respectively, at cloud cavitation. Computationally, progress has been made in Navier–Stokes (N–S) based solution techniques. Issues including suitable algorithm development for treating large density jump across phase boundaries, turbulence and cavitation models, and interface tracking are discussed. While satisfactory predictions in wall pressure distribution can be made in various cases, aspects such as density and stress distributions exhibit higher sensitivity to modeling details. A perspective of future research needs in computational modeling is offered. © 2001 Elsevier Science Ltd. All rights reserved.

---

## Contents

1. Introduction . . . . .	552
2. Experimental investigation . . . . .	553
2.1. Incipient cavitation in non-separated flows ( $\alpha = 8^\circ$ and $\sigma = 1.60$ ) . . . . .	554
2.2. Sheet cavitation . . . . .	556
2.3. Cloud cavitation . . . . .	558
2.4. Supercavitation ( $\sigma = 0.40$ , $\alpha = 8^\circ$ ) . . . . .	559
2.5. Velocity profiles, and lift and drag coefficients . . . . .	565
3. Computational modeling . . . . .	566
3.1. Dynamics and governing equations at a phase-change interface . . . . .	568
3.2. Derivation of Rayleigh–Plesset equation . . . . .	569

---

\*Corresponding author. Tel.: +1-352-392-0961; fax: +1-352-392-7303.  
E-mail address: wei-shyy@ufl.edu (W. Shyy).

3.3. Cavitation inception and cavitation parameter . . . . .	569
3.4. Governing equations and transport equation based cavitation modeling . . . . .	569
3.5. Assessment between computation and experiment . . . . .	574
4. Summary and conclusions . . . . .	577
Acknowledgements . . . . .	579
References . . . . .	579

## 1. Introduction

In liquid flows, cavitation generally occurs if the pressure in certain locations drops below the vapor pressure and consequently the negative pressures are relieved by means of forming gas filled or gas and vapor filled cavities [1]. Cavitation can be observed in a wide variety of propulsion and power systems like pumps, nozzles, injectors, marine propellers, hydrofoils and underwater bodies [2]. Cavitating flows in most engineering systems are turbulent, and the dynamics of the interface formed involves complex interactions between vapor and liquid phases. These interactions are not well understood in the closure region of the cavity where a distinct interface may not exist and the flow is unsteady. Undesirable features of cavitation are structural damage, noise and power loss. On the other hand, drag reduction can be observed on bodies surrounded fully or partially with a natural or gas ventilated cavity [3].

Numerous aspects of cavitation have been studied by many investigators during the last several decades [2–5]. With a given Reynolds number and incidence angle, incipient cavitation, sheet cavitation, cloud cavitation, and supercavitation appear in response to the cavitation number. Different combination of these control parameters result in complicated flow structure and cavitation characteristics.

Among the notable studies, Arakeri and Acosta [6] have investigated this flow regime using two axisymmetric bodies with the Schlieren flow visualization method. They found that incipient cavitation occurs within the region of separated flow, and that the point of laminar separation and the leading edge of the cavity are closely correlated. Furthermore, the distance between these two locations appears to be strongly dependent on the Reynolds number [7]. In separated flow regions, the incipient cavitation is influenced by the mixing layer eddy [8,9] specifically, the axial secondary shear layer structure [10]. It is clear that there is a close relation between the turbulent flow field and the cavitation phenomena around bodies with large flow separation. In the case of non-separating flow around a 2-D hydrofoil, as summarized by Rood [11], bubble distortion for traveling bubble cavitation in

which bubbles exhibited twin tail streaming from the bubbles is observed in the cavitation inception state. The distortion of the bubble is visually consistent with the presence of horseshoe vortices in the flow, with the bubble in the loop and the tails entrained in the vortex legs. Overall, we have inadequate understanding of the interaction between turbulent flows and cavitation inception.

With parameters such as the Reynolds number, geometry, and the incidence angle fixed, attached cavitation develops when the cavitation number is lowered from that for incipient cavitation, taking the form of a sheet [12]. Most of the previous studies of sheet cavitation focus on the behavior of the leading and trailing edges. The leading edge of a sheet cavity typically exhibits a finger-like structure [13]. The location of cavity detachment is a function of the free stream Reynolds number and the cavitation number [14,15]. The sheet cavitation is often accompanied by a highly unsteady trailing edge. Pham et al. [16] have identified two sources of sheet cavitation instability: the re-entrant jet and small interfacial wave. Although extensive observations of attached sheet cavities have been reported, there is little information about the dynamics of a sheet cavity. In particular, more insight is needed to elucidate the physical mechanisms responsible for the formation of the finger-like structure in the leading edge and the unsteady characteristics of the trailing edge.

In a related topic, Li and Ceccio [17] have conducted an experiment to investigate the traveling bubbles, each individually created by a single nucleus, interacting with boundary layers. The bubbles are found to generate local regions of turbulence and can temporarily sweep away a portion of attached cavitation. Briancon-Marjollet et al. [18] have also investigated experimentally transient bubbles interacting with an attached cavity, with emphasis on the mechanisms related to exploding bubbles and boundary layers.

Further decreasing the cavitation number, the trailing edge becomes increasingly unsteady, and cloud cavitation is formed. In cloud cavitation, vortex shedding into the downstream flow field appears at certain frequencies. Of the various cavitation phenomena, cloud cavitation causes more vibration, noise and erosion [9,19]. Furness

and Hutton [20] first suggest that the re-entrant jet is the principal mechanism of cloud cavitation, which is confirmed by Kubota et al. [21], Le et al. [22], and Kawanami et al. [23]. However, Avellan et al. [24] propose that laminar-turbulent transition in the boundary layer and growth of instability on the cavity surface can generate cloud cavitation. Gopalan and Katz [13] report that when the cavity is thin there is no-reverse flow detected in the downstream of a cavity. Instead, the cavities collapse as the vapor condenses, creating in the process hairpin-like vortices with microscopic bubbles in their cores. Therefore, the generation mechanism of cloud cavitation may not be unique, and has not been settled.

Supercavitation is the final state of cavitation. In this regime, the pressure in cavitating area is low and a big fixed cavity is formed. Compared with other types of cavitation, the interface of a supercavitation cavity is stable. Based on the potential flow analysis, a free stream theory has been developed by Wu and Wang [25]. Related to this theory, Oba and Ikohagi [26] have proposed an analysis method based on the momentum theorem for flows around cascade of hydrofoils. Furuya and Acosta [27] have calculated the pressure distribution around a supercavitating hydrofoil with a rounded nose using the potential flow theory along with singular perturbation techniques. All of numerical studies are based on the same 2-D physical model, where the pressure in a supercavitation cavity is uniform and equals to the vapor pressure. The interface of the cavity coincides with a streamline, and is smooth. However, as observed by Oba and Ikohagi [28], the assumption of “smooth separation” is not satisfactory because the flow can detach from the separation point abruptly. These models have not fully accounted for the main features related to supercavitation.

In recent years, supercavitation has attracted growing interests due to its potential for vehicle maneuvering and drag reduction. Recent accounts of the various aspects can be found in an article in Scientific American by Ashley [29] and materials collected for a lecture series on supercavitation at von Karman Institute (VKI) of Fluid Dynamics [30]. In particular, the VKI lecture notes contain comprehensive overview and historical development (by Michel [31] and Tulin [32]), experimental observations of steady state and time-dependent dynamics of cavities (by Michel [33], Stinebring et al. [34] and Kirschner [35]), formulation and analytical treatments (by Tulin [32], Garabedian [36], Vasin [37], Fridman and Achkinadze [38], Vasin [39], and Rozhdestvensky [40]), simplified computational techniques (by Kirschner [41] and Semenko [42]), Navier–Stokes (N–S) based computation (by Kunz et al. [43]), and propulsion and propeller considerations (Tulin [32], Savchenko [44], Achkinadze [45], and Kinnas [46]).

Currently, four research areas are being focused on to explore the benefit of supercavitation: (1) understanding of supercavitation physics, (2) development of modeling and computational tools, (3) development of control methodology, such as cavitator, control surfaces, and control algorithms, and (4) hydroacoustics related to sensor and signal processing. This is an active area containing extremely challenging technical issues.

In the present paper, we offer a review of the experimental and computational efforts made in understanding and predicting the dynamics of attached, turbulent cavitating flows. The focus on the experimental side is on the evolution and characteristics of the various flow regimes in accordance with specific combinations of the Reynolds number, incidence angle, and cavitation number. For simplicity, the cavitation number is adopted as the primary control parameters with other parameters held unchanged. The materials with experimental content are largely based on the work of Takenaka [47] Liu et al. [48] and Wang [49]. On the computational side, recent progress made in developing N–S-based solution techniques, aided with engineering closures for turbulence and cavitation, is highlighted. While the current predictive capability is not mature for complex cavitating flow structures, key parameters such as pressure distributions around an object can often be predicted reasonably well. We will also discuss the outstanding issues from both physical modeling and computational algorithm viewpoints, including non-equilibrium turbulence structure, interfacial dynamics, moving boundaries, and appropriate techniques to handle both compressible and incompressible flow regimes using either a pressure-based or a density-based approach.

## 2. Experimental investigation

Based on the work of Takenaka [47], Liu et al. [48] and Wang [49] we outline the major cavitation regimes under the various combinations between incidence angle and cavitation number. Salient features of different types of cavitation are observed using a high-speed video camera. The video camera can attain a rate of 40,500 frames/s. However depending on the fluid velocity and the area to be visualized, lower rates are often preferable. The visualization is conducted from both top and side directions of the Clark-Y hydrofoil, on a laser beam sheet. Laser Doppler velocity (LDV) is employed for velocity measurement. The focus is on discernible characteristics of the flow field associated with various cavitation regimes, and their influences on the subsequent development of the cavitation dynamics. Velocity profiles and overall lift and drag coefficients are documented in a number of cases to offer a quantitative

Table 1

Summary of the dynamic processes of incipient cavitation. A total of 23 events are listed below. The positions of onset, maximum-size, and complete collapse of the hairpin cavitating structure, as well as the time duration between these points are given

Event No	A: Position of onset for forming cavitating hairpin structure ( $l/c\%$ )	B: Position that cavitating hairpin structure reaches maximum size ( $l/c\%$ )	Time duration between A and B (ms)	C: Position that cavitating hairpin structure collapses ( $l/c\%$ )	Time duration between B and C (ms)
1	13.7	37.0	1.33	43.6	0.44
2	8.8	48.6	2.44	55.4	0.67
3	12.3	47.2	2.22	52.1	0.44
4	12.6	40.4	1.78	45.8	0.44
5	11.6	41.1	1.78	49.3	0.67
6	11.6	42.5	1.78	48.6	0.67
7	13.7	42.5	1.78	45.9	0.44
8	13.7	41.8	1.78	45.6	0.44
9	11.6	44.5	2.00	50.7	0.67
10	11.6	39.0	1.56	45.9	0.44
11	11.6	39.0	1.56	46.6	0.67
12	11.6	39.7	1.78	44.5	0.44
13	12.3	39.0	1.56	46.6	0.67
14	12.3	39.7	1.56	43.2	0.44
15	12.3	40.4	1.56	47.3	0.67
16	11.0	42.5	2.00	52.1	0.67
17	12.3	42.5	1.78	50.0	0.89
18	13.7	43.2	1.78	47.9	0.44
19	11.6	42.5	1.78	47.3	0.44
20	13.0	45.9	2.00	51.4	0.67
21	11.6	42.5	2.00	50.1	0.67
22	12.3	41.8	1.78	45.9	0.67
23	12.3	42.5	1.78	50.1	0.67
Average	12.2	42.0	1.80	48.1	0.57

basis, in addition to the extensive visualization information, to further our understanding of the cavitating flow structures. In the results reviewed below, the Reynolds number is fixed at a value of  $7.0 \times 10^5$  while systematically varying the cavitation number to explore the structure of the unsteady cavitating flow. It is known that cavitation doesn't simply scale with Reynolds number, cavitation number, and the incidence angle. However, within the limited scope of this review, we will not cover other issues. The cavitation parameter is typically defined as follows:

$$\sigma = \frac{2(P_\infty - P_v)}{\rho U_\infty^2}. \quad (1)$$

In the following, we review the salient features of the various cavitating flow regimes. The results are based on the study of the Clark-Y hydrofoil, and are meant to convey a sense of dynamic evolution of the flow characteristics. While with different solid objects and flow environment, the quantitative details will vary, the key features discussed below should hold true in general.

### 2.1. Incipient cavitation in non-separated flows ( $\alpha = 8^\circ$ and $\sigma = 1.60$ )

Fig. 1 shows time evolution of the cavitating flow in the incipient cavitation stage, with non-separated flows. In the case shown, the cavitation number is 1.60. The sequence begins with the formation of a pair of clustered micro-sized bubbles at about 10% chord length from the leading edge of the hydrofoil. In the photographs, the cavitating flow appears in white, indicating that it contains a number of micro-sized vapor bubbles. In other words, the incipient cavitation appears as a collection of bubbles at the very early stage. In the subsequent frames, from  $t = 0.22$  to 1.56 ms, the cavitating flow grows noticeably, forming a hairpin-shaped structure. Furthermore, the velocity field surrounding the hairpin-structure convects in a contra-rotating manner, with the fluid between the two legs moving away from the wall. The figure suggests that the cavitation inception in non-separated turbulent flow is related to the coherent structures in the boundary layer. Such a flow structure can make a marked contribution

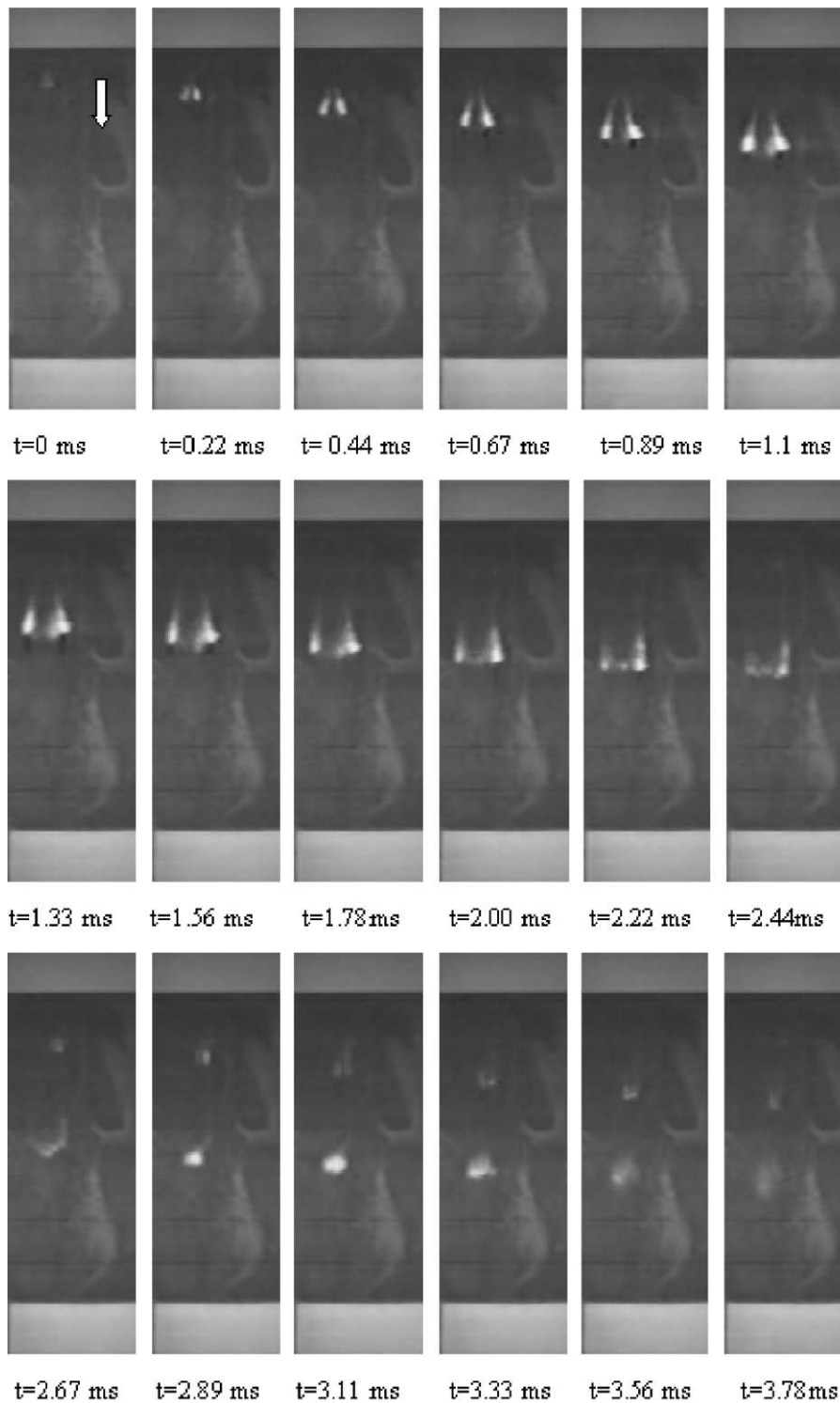


Fig. 1. Time evolution of a representative cavitating hairpin structure in the inception cavitation phase. (The arrow in the figure is the flow direction.) ( $\sigma = 1.60$ ,  $\alpha = 8^\circ$ ).

to the Reynolds stress. For non-cavitating flows, the occurrence of the hairpin-shaped vortex structure in the near-wall region has been well established [50–53]. It is clear that turbulent bursting and the hairpin-shaped vortex structure accompany the incipient cavitation. One cannot say for sure whether the bursting mechanism is responsible for the incipient cavitation; however, the fluctuating pressure field associated with turbulent bursting seems to be a reasonable candidate to at least promote the observed cavitating flow structure.

In Fig. 1, at  $t = 1.78$  ms, the hairpin-shaped structure grows to the maximum size. The frames from  $t = 2.00$  ms and beyond show the collapsing process of the hairpin-structure. In the process, first, the two legs reduce in size, while the number of bubbles in the spanwise direction increase, as shown in frames  $t = 2.22$  and  $2.44$  ms. Next, the bubbles collapse, as shown in frame  $t = 2.67$  ms; they then reappear, grow in size until  $t = 3.33$  ms, and then collapse again. However, the reemerged cavitating flow does not form a hairpin structure anymore. A different description of the observed cavitating structure has been given by Rood [11]. Rood has suggested that the formation of the hairpin (which he called horseshoe) flow structure is caused as a cavitating bubble is dragged through the boundary layer by the higher velocity in the outer layer, producing trailing vortices entraining the bubble as the boundary layer vorticity is rolled up and turned in the streamwise direction. In our study, many micro-sized bubbles are contained in the cavitating hairpin structure. Furthermore, as shown in Fig. 1, the cavitating hairpin can collapse, and the re-emerged cavitating flow does not assume a hairpin shape. These

observations indicate that the hairpin structure does not seem to result from a distorted bubble due to the velocity profile in a boundary.

A number of incipient cavitation events are summarized in Table 1. Fig. 1 corresponds to the Event No. 17 in Table 1. In Fig. 1, we define frame 1 ( $t = 0$  ms) as the point of onset for the formation of the hairpin-structure, frame 9 ( $t = 1.78$  ms) as the point reaching the maximum size of the hairpin-structure, and frame 13 ( $t = 2.67$  ms) as the point of collapse of the hairpin-shaped cavity. Table 1 indicates that, with the given Reynolds number and the geometric configuration, the hairpin-shaped cavitating structures travel downstream, while exhibiting repetitive onset-growth-collapse processes.

Fig. 2 depicts time evolution of the length of the cavitating hairpin vortex, non-dimensionalized by the chord length (70 mm). Three cases, corresponding to the events 21, 22 and 23 in Table 1, are shown in the figure. The aforementioned onset-growth-collapse process is clearly illustrated. The trends between repetitive events are also consistent.

## 2.2. Sheet cavitation

### 2.2.1. Formation of sheet cavitation

Further lowering the cavitation number, the cavitation changes from the incipient cavitation to a sheet-like cavity. Comparing Fig. 1 ( $\sigma = 1.60$ ) and Fig. 3 ( $\sigma = 1.55$ ), one observes that as the cavitation number is lowered, more cavitating vortex pairs appear. The number of bubbles contained in each vortex pair also increases. Fig. 3 shows the time evolution of a transitional process from incipient cavitation to sheet cavitation. The length scale of the vortex pair in Fig. 3 is larger than that observed in Fig. 1, with more bubbles inside. At  $t = 1.33$  ms, an additional, smaller cavitating vortex pair appears between the two original vortices, leading to the formation of a new hairpin-shaped structure. At  $t = 2.67$  ms, the cavitating vortices are attached to the surface of the hydrofoil, and the initial traveling cavities now expand into a sheet cavity. Because the sheet cavity develops from the attachment of individual cavitating vortices, the liquid-vapor interface is of a finger-like structure. Similar findings are also reported by Gopalan and Katz [13], albeit with different levels of details.

### 2.2.2. Unsteady characteristics of sheet cavitation

When the cavitation number is reduced to 1.40, as shown in Fig. 4, the leading edge of a sheet cavity exhibits a finger-like structure. As described, such a shape is due to the combination of different vortex pairs, and detachment of the head of each pair. Although the cavity is attached, the rear region of the sheet is unsteady, 3-D, and rolls up into a series of bubbly

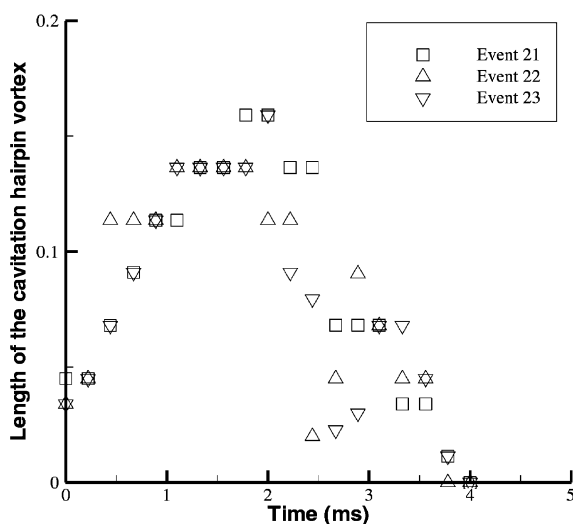


Fig. 2. Time evolution of the length of the cavitation hairpin vortex. (Non-dimensionalized by the chord length. Three events are shown here.)

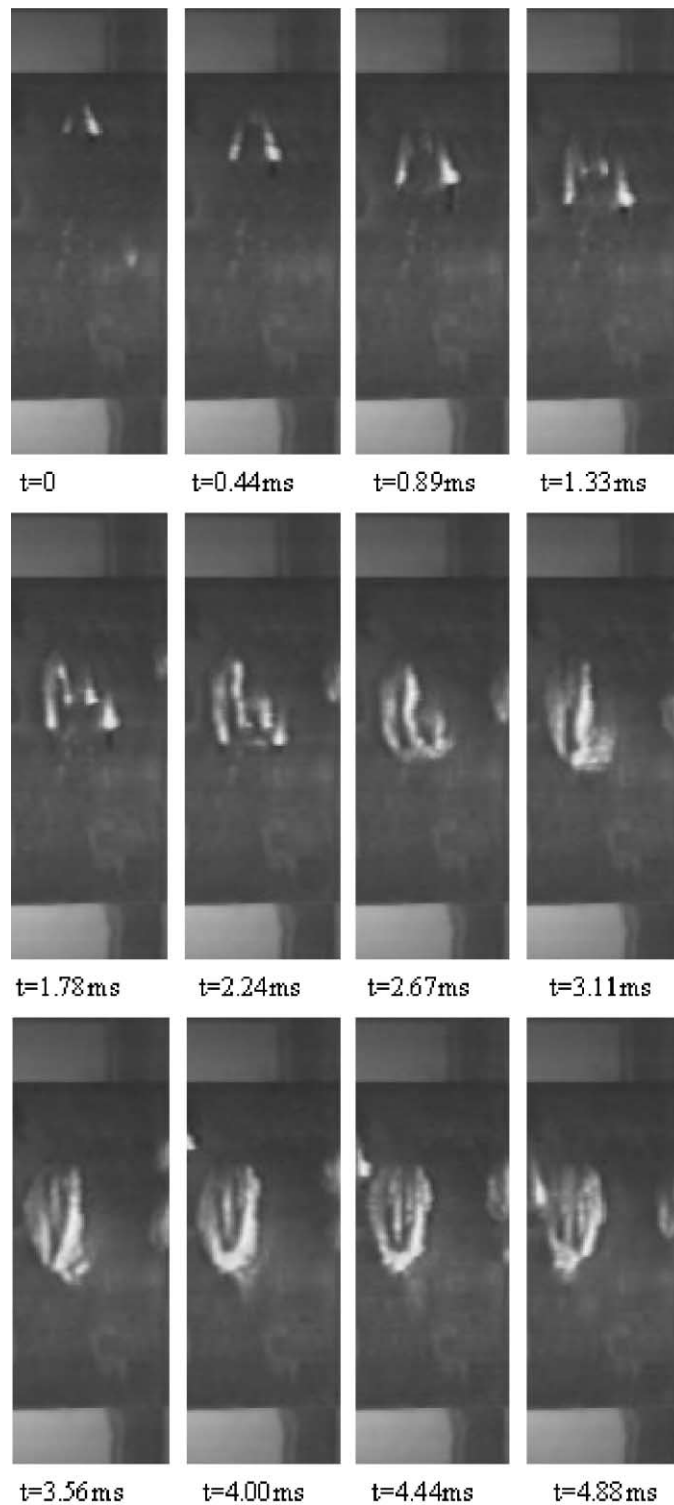


Fig. 3. Transition process from incipient cavitation toward sheet cavitation, with the cavitating flow becoming attached while forming a sheet cavity ( $\sigma = 1.55$ ,  $\alpha = 8^\circ$ ).

Table 2  
Comparisons of observed vortex shedding dynamics of cloud cavitation

Reference	$Re$	Cavitation number	Velocity (m/s)	Incidence	Shedding frequencies (Hz)
Present work	$7.0 \times 10^5$	0.80	10	$8^\circ$	20
Kawanami et al. [23]	$7.2 \times 10^5$	1.07	5	$6^\circ$	20
Pham et al. [16]	$1.2 \times 10^6$	1.2	8	$4^\circ$	29

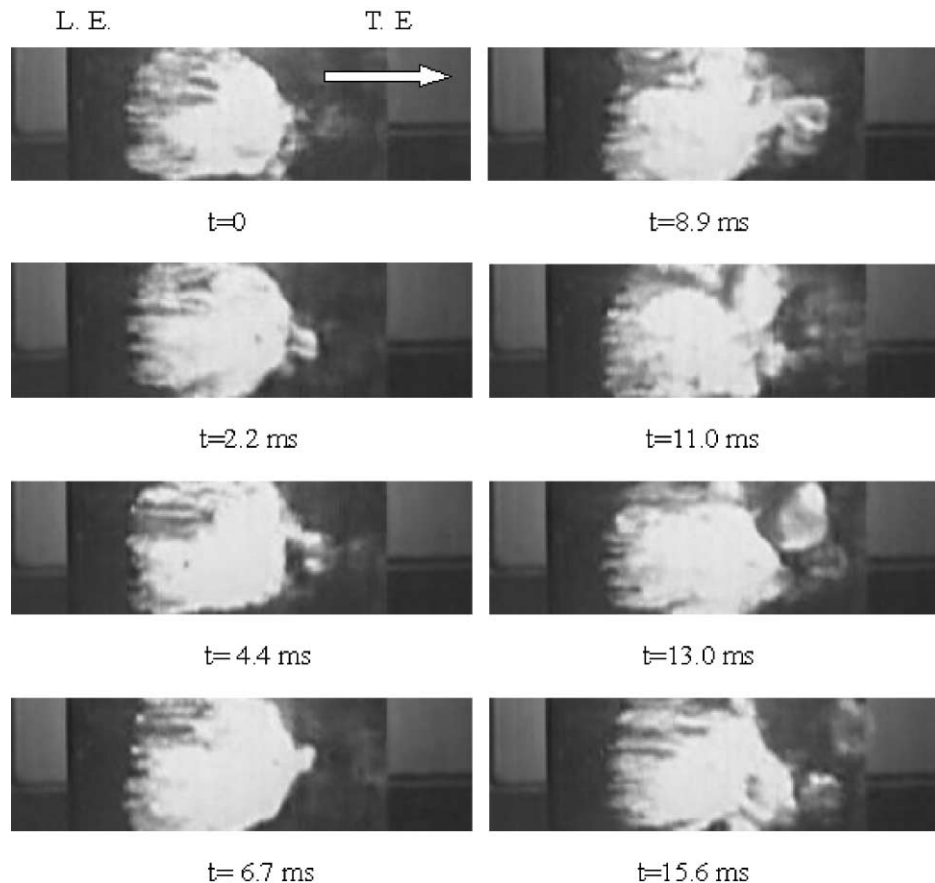


Fig. 4. Top view of the development of a sheet cavity. (The arrow in the figure is the flow direction) ( $\sigma = 1.40$ ,  $\alpha = 8^\circ$ ).

eddy that are shed intermittently. To understand the unsteady characteristics of the sheet cavitation more clearly, the leading and trailing edge positions of a sheet cavity at the mid-span of the hydrofoil, at two cavitation numbers, are measured. As shown in Fig. 5, the positions of the leading edge of a cavitating sheet remain largely fixed in both cases. However, the trailing edge positions change more substantially in time, indicating that the unsteady behavior of a sheet cavity appears predominantly in the rear region of a cavity.

### 2.3. Cloud cavitation

Further decreasing the cavitation number, the sheet cavitation grows and the trailing edge becomes increasingly unsteady. Accompanying this trend, bubbles are shed massively in the rear portion of the cavity, and the cloud cavitation is formed. It is observed that cloud cavitation has a distinctly quasi-periodic pattern. Figs. 6 and 7 show the visualization results from both top and side views, within a single cycle of the events. Estimated from the video images, the frequency of the cloud



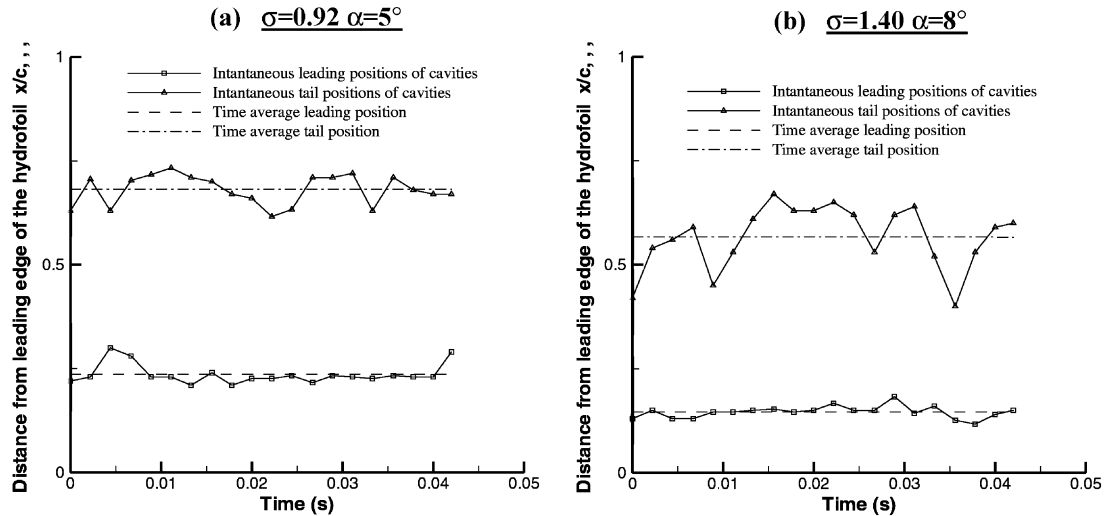


Fig. 5. Time evolutions of the leading and trailing positions of sheet cavities.

cavitation under the given parameters is about 20 Hz, which leads to a Strouhal number, based on the mean length of the cavity and free stream velocity, of 0.1. Table 2 shows that the listed frequency is comparable to those reported by Kawanami et al. [23] and Pham et al. [16].

As shown in Fig. 6, in cloud cavitation, the development of the cavity is qualitatively similar to that of sheet cavitation, namely, an attached front portion and an unsteady rear region. As shown in Fig. 6 at  $t = 0$ , immediately after a vortex shedding event takes place, the cavity is attached. The cavity grows in time, while traveling downstream, with packets of bubbles (as evidenced by the bright colored regions in Fig. 6) moving with a clockwise rotation. The rotating direction can be deduced by the influence of the free stream flow direction, as well as the images shown in Fig. 7. Supporting observation has also been reported by Kawanami et al. [23]. In the near wall region, due to the reduced fluid velocity and higher pressure, caused by the large-scale vortex dynamics, the cavitating flow is pushed away from the wall. Associated with the departing vortical flow, one observes substantial growth of the cavity thickness in the rear region of the cavity.

To further illustrate the development of the flow structure, close-up views in the rear region of the hydrofoil are depicted in Fig. 8. It shows that the cavitating flow grows till about the midpoint of the cycle,  $t = 27.8$  ms, before the massive vortex shedding appears (see the image at  $t = 33.3$  ms). Accompanying the large-scale vortex dynamics, shown at  $t = 33.3$  ms, a re-entrant flow in the wall region is

induced toward the upstream. Kawanami et al. [23] have also found a similar re-entrant flow structure during the second half of the cycle. The propagation velocity of the re-entrant flow is estimated to be  $1.0 \pm 0.13$  m/s, based on the analysis of the pictures, which is about 10% of the free stream velocity. This result is consistent with that of Pham et al. [16]. As shown in Figs. 6 and 7, as the re-entrant flow reaches the vicinity of leading edge of the cavity, the existing cavitating flow is pushed away from the wall, and a new cavitating flow structure forms there.

The importance of the re-entrant flow on the shedding and collapse of the large-scale cavitating vortex structure has been mentioned by previous researchers [20,22,23,54]. Figs. 6 and 7 indicate that the shedding of cavitating vortices is mainly responsible for the quasi-periodic characteristics of cloud cavitation. Fig. 9 shows the time evolution of leading and trailing edge positions of the present cloud cavitation case. Comparing Fig. 5 and Fig. 9, as expected, the trailing edge position in cloud cavitation changes more substantially with time than that in sheet cavitation. This is the reason why the cloud cavitation induces stronger structural vibration and noise. Fig. 10 shows the time evolution of the cavity thickness at different chord positions. Two different cavitation numbers and angles of attack are included. In both cavitation states, the largest fluctuation of cavity thickness takes place around the 80% chord position.

#### 2.4. Supercavitation ( $\sigma = 0.40$ , $\alpha = 8^\circ$ )

Supercavitation is the final state of cavitation, which is caused by further decreasing the cavitation

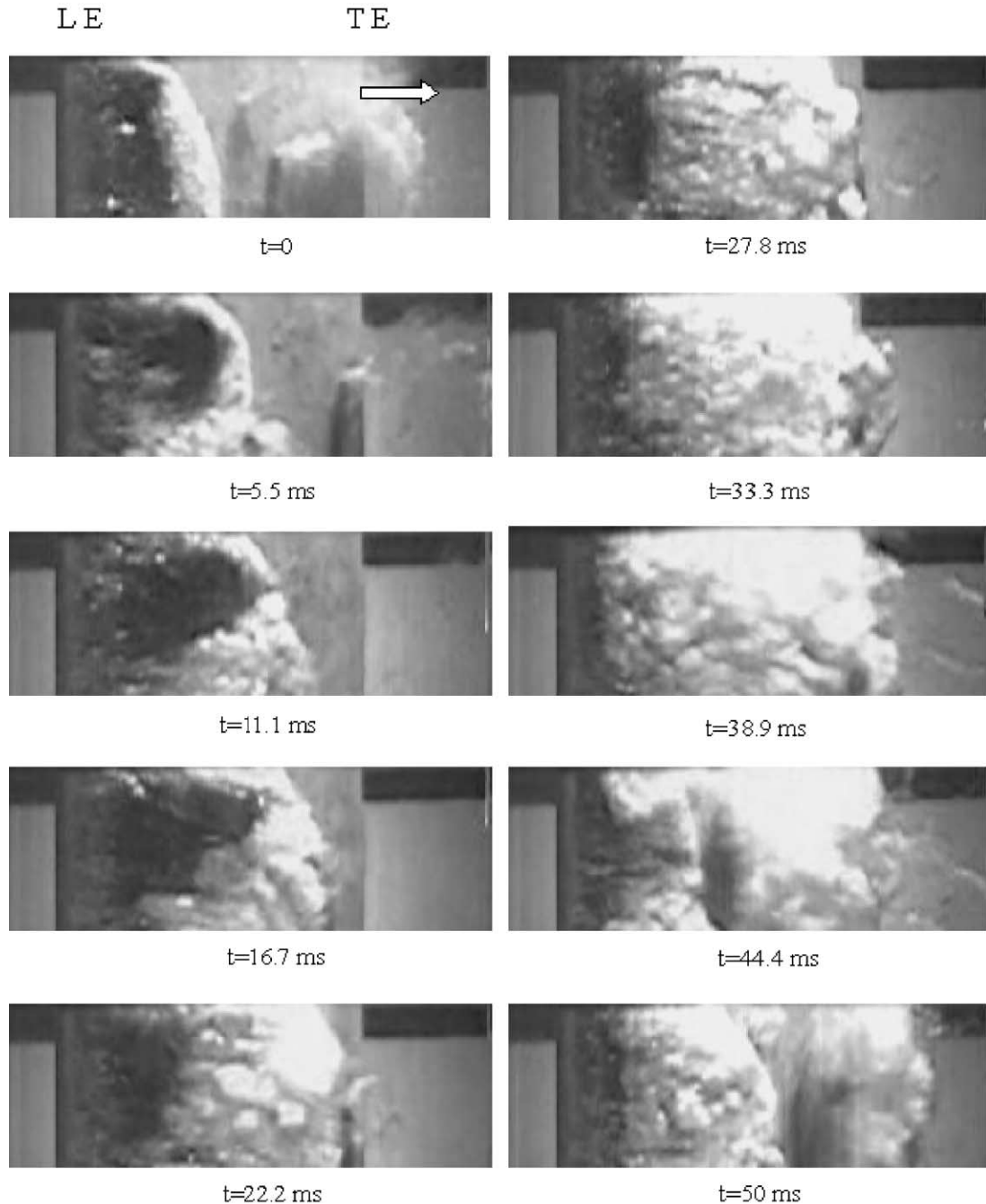


Fig. 6. Time evolution of cloud cavitation from the top view ( $\sigma = 0.80$ ,  $\alpha = 8^\circ$ ).

number from the cloud cavitation regime. Fig. 11 shows images of the flow structure corresponding to the supercavitation regime. Due to the very low pressure, the cavitating area covers the entire hydrofoil, extending to the downstream region of the solid object. There is a distinct interface be-

tween the main flow and the supercavitating region. The cavity is not filled with vapor; instead, it consists of vapor and liquid mixtures. The cavity flow experiences substantial velocity gradients. Fig. 12 shows the time averaged velocity distribution at different chord positions, obtained by LDV measurements reported

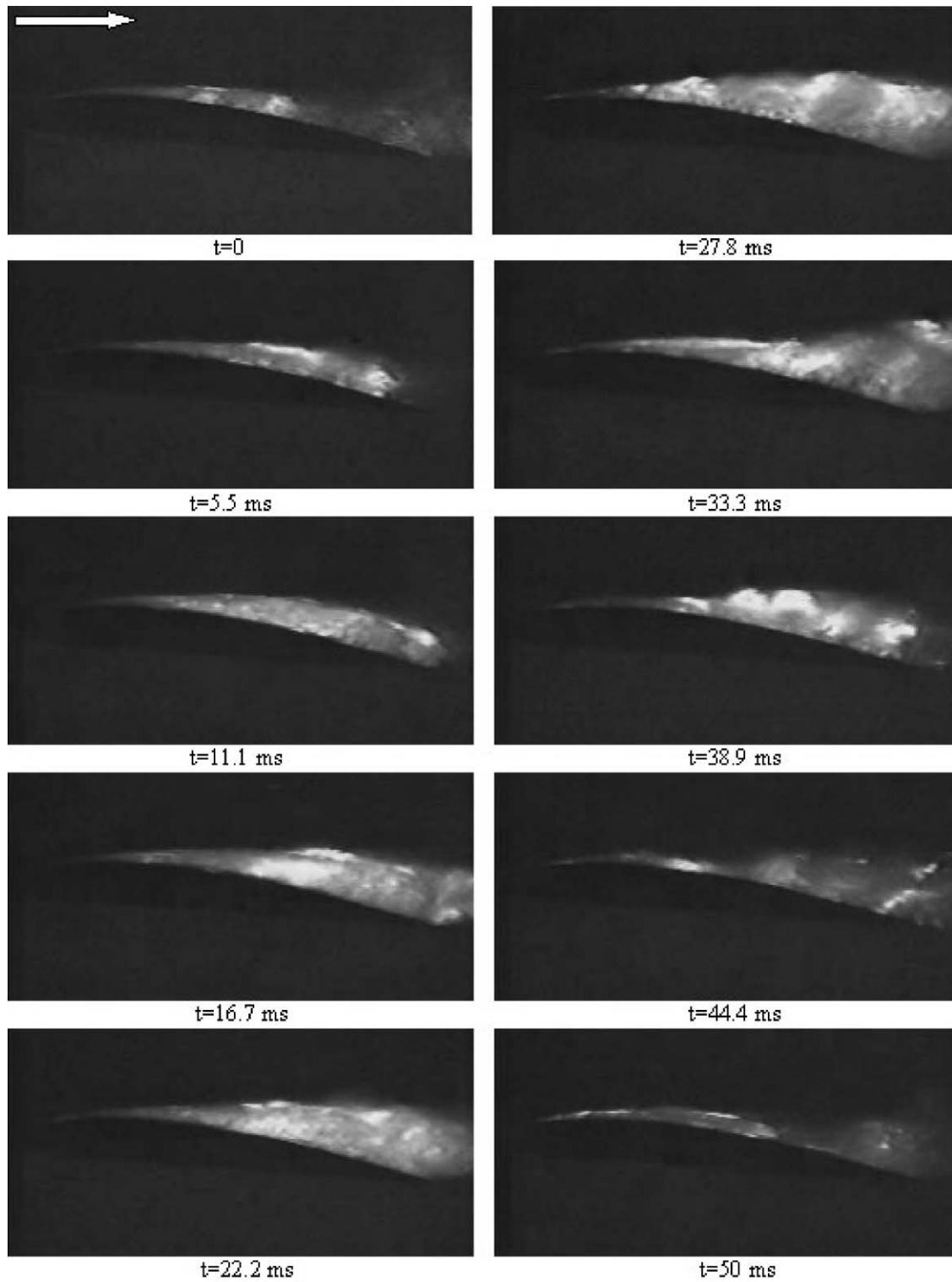


Fig. 7. Time evolution of cloud cavitation from the side view ( $\alpha = 8^\circ$ ,  $\sigma = 0.80$ ).

Table 3

Overview of selected studies on numerical simulations of cavitating flows based on the solution of N–S equations

Reference	Cavitation model	Numerical algorithm	Applications/main findings
Kubota et al. [54]	Rayleigh–Plesset equation coupled to the Poisson equation. Cavity region is modeled as compressible fluid with variable density	Marker and cell, 3-D N–S equations, no turbulence model	Cloud cavitation on hydrofoils. Numerical instability for high-density ratio. $Re = 3 \times 10^5$
Chen and Heister [57]	Interface tracking based on $P = P_{\text{vap}}$ Grid conforms to the cavity shape	Marker and cell, 2-D N–S equations, no turbulence model	Pressure distribution on axisymmetric geometries. $Re = 1.36 \times 10^5$
Chen and Heister [60]	Time and pressure dependent pseudo-density equation	Marker and cell, 2-D N–S equations, no turbulence model	Pressure distribution on axisymmetric geometries. $Re = 1.36 \times 10^5$
Deshpande et al. [58]	Interface tracking based on $P = P_{\text{vap}}$ with mass transfer. Grid conforms to the cavity shape	Artificial compressibility, 2-D N–S equations, no turbulence model	Sheet cavitation for cryogenic fluids. Studied the thermal boundary layer over cavity
Singhal et al. [65]	Vapor mass fraction equation with pressure dependent source terms	Pressure-based, 2-D N–S equations, $k - \varepsilon$ turbulence model	Pressure distribution and discharge coefficient for orifices and hydrofoils. $Re = 2 \times 10^6$
Merkle et al. [66]	Vapor mass fraction equation with pressure dependent source terms	Artificial compressibility, 2-D N–S equations, two equation turbulence model	Pressure distribution on hydrofoils.
Kunz et al. [67,68]	Volume fraction equation with pressure dependent source terms Non-conservative continuity equation. Preconditioning strategy	Artificial compressibility, 3-D N–S equations, $k - \varepsilon$ turbulence model	Pressure distribution on axisymmetric geometries. $Re = 1.36 \times 10^5$
Ahuja et al. [69]	Vapor mass fraction equation with pressure dependent source terms. Preconditioning strategy. Adaptive unstructured meshes	Artificial compressibility, 3-D N–S equations, $k - \varepsilon$ turbulence model	Simulations of cavitating flow over hydrofoils ( $Re = 2 \times 10^6$ ) and axisymmetric geometries. ( $Re = 1.36 \times 10^5$ )
Edwards et al. [62]	Temperature distribution is computed to determine density variation based Sanchez–Lacombe equation of state	Artificial compressibility, 3-D N–S equations, Spalart–Allmaras one-equation model	Pressure distribution on axisymmetric geometries. Reported poor convergence and pressure overshoots $Re = 1.36 \times 10^5$
Ventikos and Tzabiras [61]	Temperature distribution is computed to determine density variation based on steam-water tables	Pressure-based, 2-D N–S equations, No turbulence model	Pressure distribution over airfoils. $Re = 2000$ in computations while $Re = 2.5 \times 10^6$ in experiments
Venkateswaran et al. [70]	Discussed the preconditioning strategies utilized in Kunz et al. and Ahuja et al.	Artificial compressibility, 3-D N–S equations, $k - \varepsilon$ turbulence model	Pressure distribution on axisymmetric geometries. $Re = 1.36 \times 10^5$
Senocak and Shyy [71]	Volume fraction equation with pressure dependent source terms. Pressure-density coupling scheme and upwinded density interpolation in cavitating regions	Pressure-based, 3-D N–S equations, different versions of $k - \varepsilon$ turbulence model	Pressure and density distribution on axisymmetric geometries. Sharp discontinuity in density at the closure region. $Re = 1.36 \times 10^5$

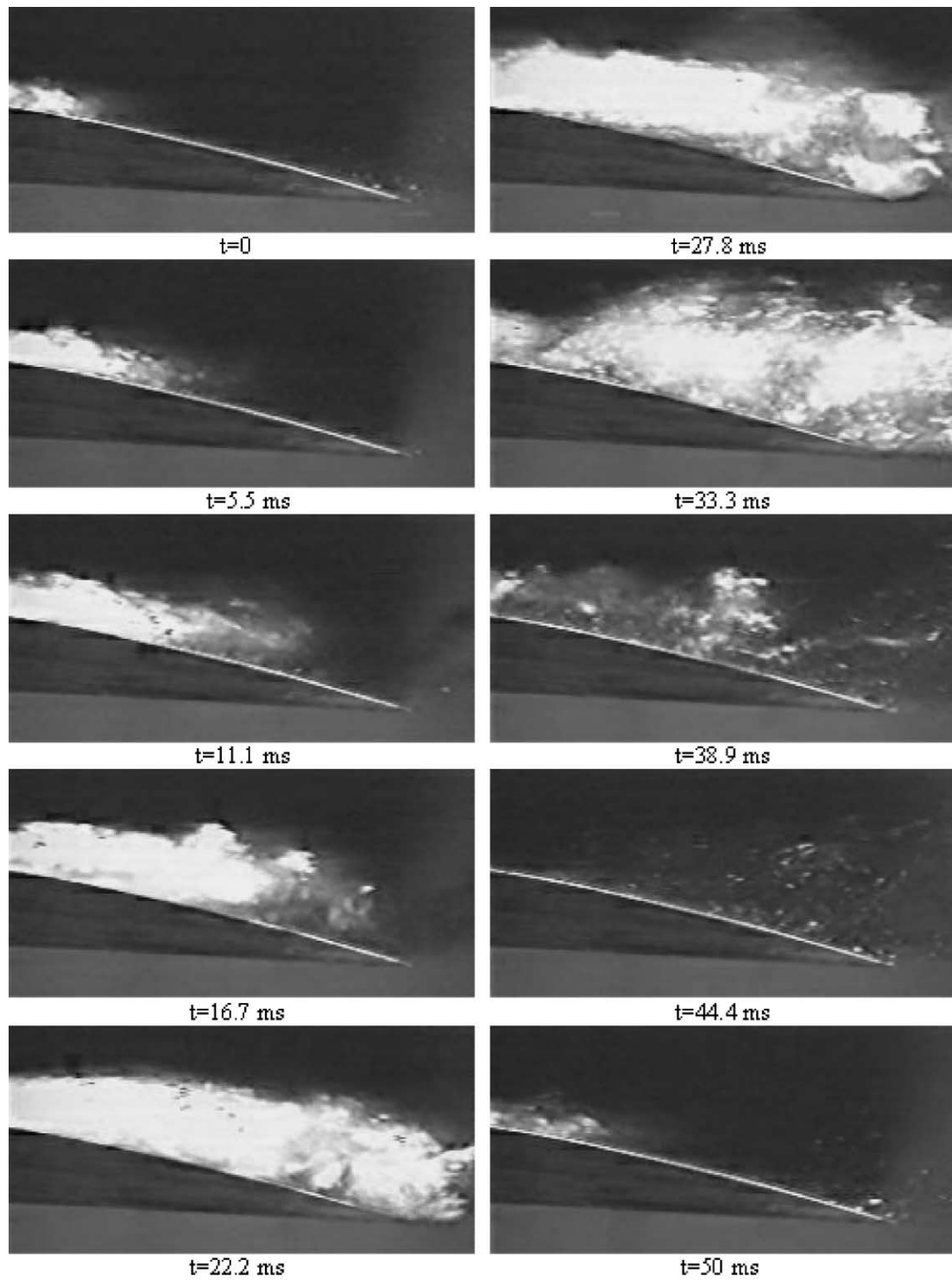


Fig. 8. Time evolution of cloud cavitation in the rear area of the foil, from the side view ( $\sigma = 0.80$ ,  $\alpha = 8^\circ$ ).

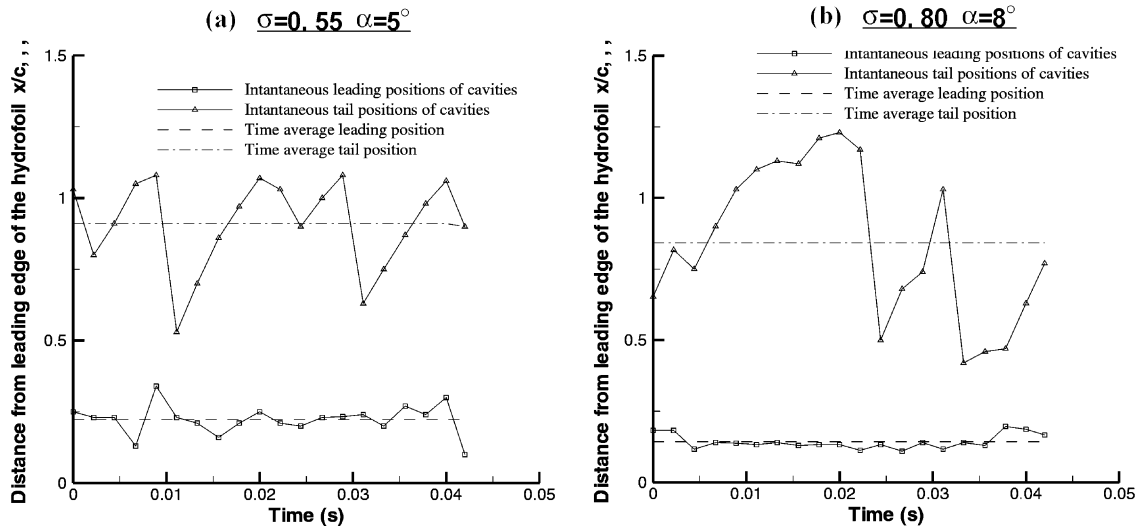


Fig. 9. Time evolutions of the leading and trailing edge positions of cloud cavitation.

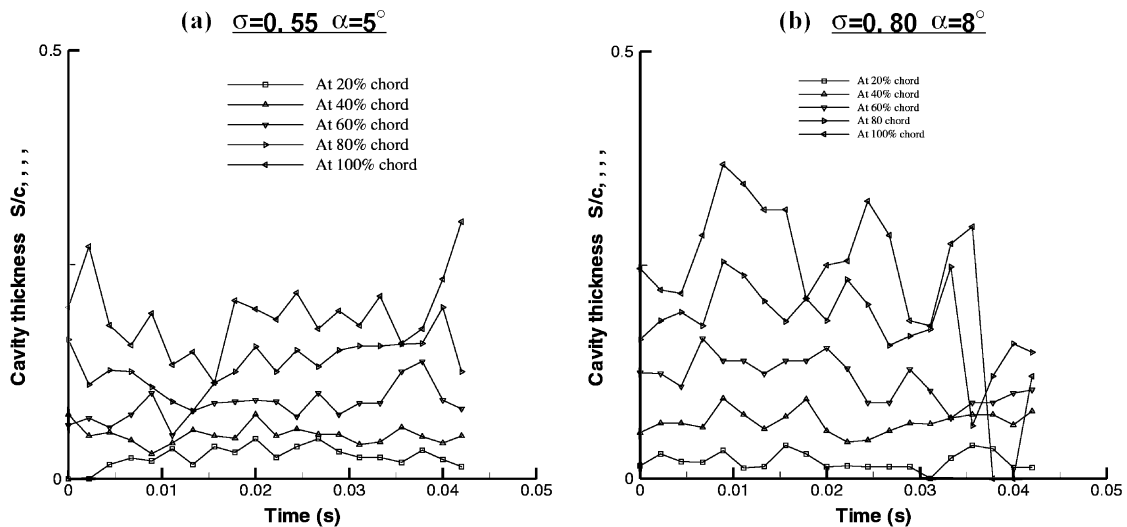


Fig. 10. Time evolutions of the thickness of cloud cavitation at different chord positions.

in Takenaka [47] and Liu et al. [48]. From the  $x$ -direction velocity profiles, one sees that the velocity of the traveling bubbles on the cavity interface is almost the same as that of the free stream; however, in the inner layer the velocity is relatively low. In Fig. 12, the solid line indicates the cavity boundary, and the traveling bubble layer is between the solid line and the dotted line.

There is no discernible, large-scale vortex motion in the supercavitating flow region. Fig. 13 shows the time evolution of a cavity thickness in different chord positions of the hydrofoil. The changes of the thickness

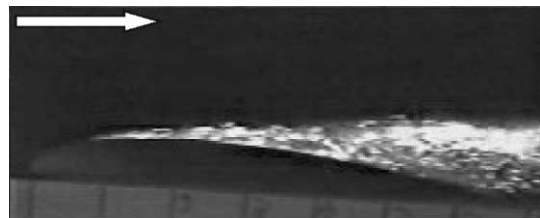


Fig. 11. Supercavitation around the hydrofoil ( $\sigma=0.40$ ,  $\alpha=8^\circ$ ).

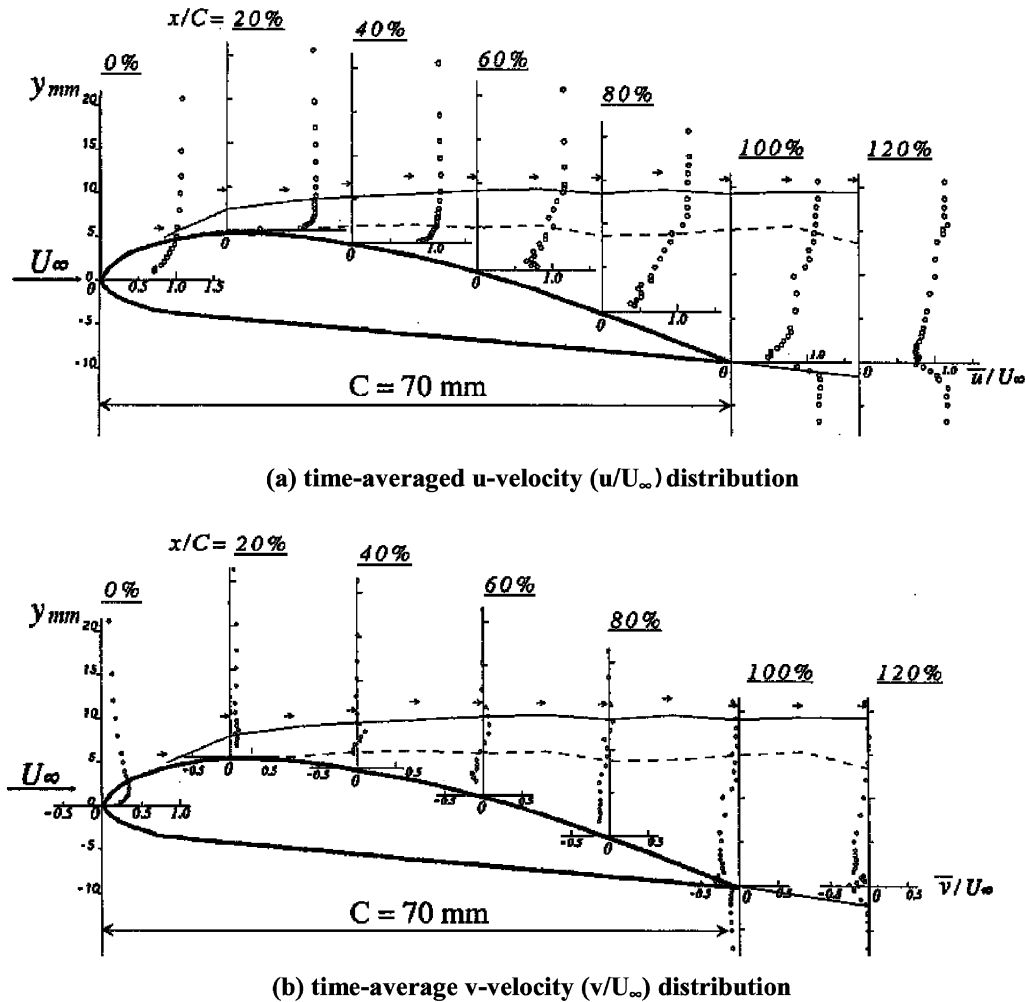


Fig. 12. Time-averaged velocity distributions in a supercavitation state. ( $\sigma = 0.28$ ,  $\alpha = 8^\circ$ ).

with time are small compared to those in cloud cavitation. Little fluctuation of the interface of supercavitation cavity is observed. A relative smooth interface of cavity is formed in the state.

### 2.5. Velocity profiles, and lift and drag coefficients

In order to gain insight into the flow structures in more details, LDV measurement has been conducted to document the mean velocity distributions in different cavitation conditions, at two incidence angles [47,48]. The results are shown in Figs. 14 and 15, where the non-dimensional streamwise velocity is scaled based on the velocity at the edge of a cavity at a given condition. The figures cover the sheet cavitation, cloud cavitation and supercavitation regimes. These two figures document that the velocity distributions inside and outside cavities are quite different. Outside the cavity, the velocity

matches the free stream condition. Inside the cavity, the velocity rapidly reduces the magnitude, exhibiting a shear layer structure. There is substantial scatter between different cavitation numbers and incidence angles.

The drag and lift characteristics of the hydrofoil in the whole operating conditions, from no cavitation to supercavitation, are summarized in Fig. 16. When the flow is non-cavitating, both the lift and drag coefficients remain largely unchanged as the cavitation number is varied. In the cavitation inception stage, cavitating flows appear as traveling cavities, as shown in Fig. 1, and the net effect of cavitation on the lift and drag coefficients is very small. Further decreasing the cavitation number, a fixed sheet cavity as shown in Fig. 4, is formed, and the drag coefficient becomes higher while the lift coefficient becomes lower. In the cloud cavitation stage, the vortex shedding and related

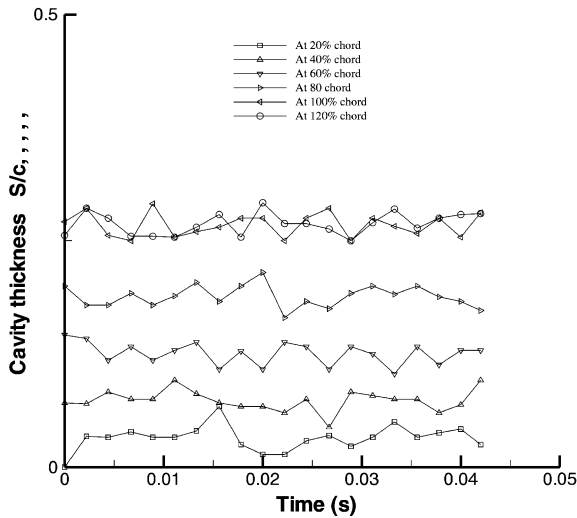


Fig. 13. Time evolution of the location of the edge of the cavity, under supercavitation, at different chord positions ( $\sigma = 0.40$ ,  $\alpha = 8^\circ$ ).

unsteady movement strongly affects the flow structure around the hydrofoil, leading to the maximum of drag and minimum of lift. Finally, while transitioning from cloud cavitation to supercavitation, the cavities exhibit more steady characteristics, and both drag and lift coefficients become lower.

### 3. Computational modeling

Computational modeling of cavitation has been pursued for years. Early studies primarily utilize the potential flow theory; they are still widely used in many engineering applications [30,41,42]. Studies dealing with cavitation modeling through the computation of the N–S equations have emerged in the last decade. An overview of selected studies is presented in Table 3. These studies can be put into two categories, namely interface tracking methods and homogeneous equilibrium flow models. In the first category the cavity region is assumed to have a constant pressure equal to the vapor pressure of the corresponding liquid and the computations are done only for the liquid phase. Constant pressure assumption is physically sensible and has been verified experimentally [55,56]. Computationally, the liquid-vapor interface can be tracked based on this assumption, along with a wake model to handle the shape of the cavity. Grid is often regenerated iteratively to conform to the cavity shape. These models are capable of simulating sheet cavitation but may not be adequate for cases where bubble growth and

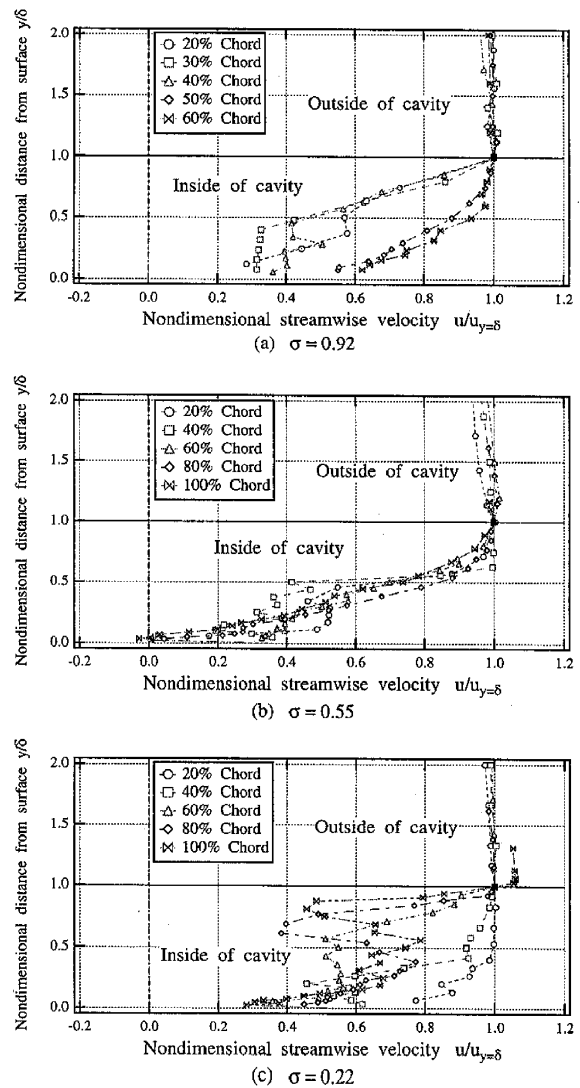


Fig. 14. The streamwise velocity distributions in various cavitating conditions ( $\alpha = 5^\circ$ ). The velocity is non-dimensionalized based on the value at the edge of the cavity. (a) sheet cavitation, (b) cloud cavitation, (c) supercavitation.

detachment exists. In addition, so far, they are limited to 2-D planar or axisymmetric flows because of the difficulties involved in tracking 3-D interfaces. Examples can be found in Chen and Heister [57] and Deshpande et al. [58]. The second category can be termed the homogeneous equilibrium flow models in which the single-fluid modeling approach is employed for both phases. Differences between the various models in this category mostly come from the relation that defines the variable density field. Delannoy and Kueny [59] utilize an arbitrary barotropic equation of state to compute the density field. Likewise, Chen and Heister [60] derive



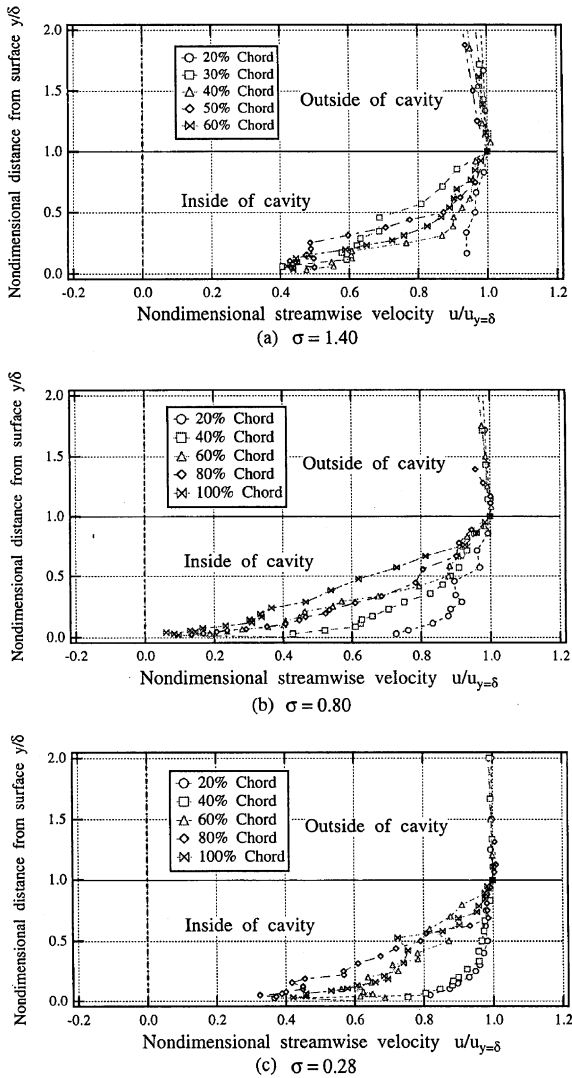


Fig. 15. The streamwise velocity distributions in cavitating conditions ( $\sigma = 8^\circ$ ). The velocity is non-dimensionalized based on the value at the edge of the cavity. (a) sheet cavitation, (b) cloud cavitation, (c) supercavitation.

a time and pressure dependent differential equation for density. Ventikos and Tzabiras [61] introduce the water-vapor state laws for this purpose. They consider the whole domain as a compressible fluid by employing the enthalpy along with the N–S equation. In a similar fashion, Edwards et al. [62] use the Sanchez–Lacombe equation of state and solve the temperature transport equation in addition to the N–S equations. Considering the isothermal character of cavitating flows in many applications, utilizing a temperature or enthalpy equation and assuming the whole flow field as compressible may not be the most effective approach. Kubota et al.

[54] couple the Rayleigh–Plesset equation [63,64] to the flow solver and compute the void fraction based on the bubble radius. Then the density is calculated using the void fraction formalism. Due to the time dependent nature of the Rayleigh–Plesset equation, the model is restricted to unsteady cloud cavitation. The authors have also reported that this method is prone to instability because of high pressure–density dependence, and could not reach the same convergence levels of non-cavitating flow simulations.

To account for the cavitation dynamics in a more flexible manner, recently, a transport equation model is developed. In this approach volume or mass fraction of liquid (and vapor) phase is convected. Singhal et al. [65], Merkle et al. [66] and Kunz et al. [67,68] have employed similar models based on this concept with differences in the source terms. One apparent advantage of this model comes from the convective character of the equation, which allows modeling of the impact of inertial forces on cavities like elongation, detachment and drift of bubbles. Merkle et al. [66] and Kunz et al. [67,68] have employed the artificial compressibility method. Kunz et al. [67,68] have adopted a non-conservative form of the continuity equation and applied the model to different geometries. Their solutions are in good agreement with experimental measurements of pressure distributions. In these studies special attention has been given to the preconditioning formulation in order to create a robust artificial compressibility method. Ahuja et al. [69] have used the same method and developed an algorithm to account for the compressibility effects in the context of artificial compressibility methods with adaptive unstructured grids. Ahuja et al. [69] have only presented the predicted cavity shapes for axisymmetric flows; their predictions seem to be noticeably different from those of Kunz et al. [67] for the corresponding flow conditions. Venkateswaran et al. [70] have compared the above-mentioned studies, and concluded that all three preconditioning formulations are essentially the same with minor differences.

Recently, there have also been papers on pressure-based methods for computing cavitating flows using the transport equation model. [65,71,72]. By pressure-based method, we mean that the pressure field is solved by combining the momentum and mass continuity equations to form a pressure or pressure-correction equation [73–75]. In Senocak and Shyy [71,72], a pressure-based algorithm with conservative formulation, multi-block, curvilinear grid systems, is adopted to compute cavitating flows. In particular, the coupling between velocity, pressure and density for proper formulation of the pressure correction equation for cavitating flow conditions has been discussed. The mass transport equation cavitation model, such as that employed by Kunz et al. [67,68]

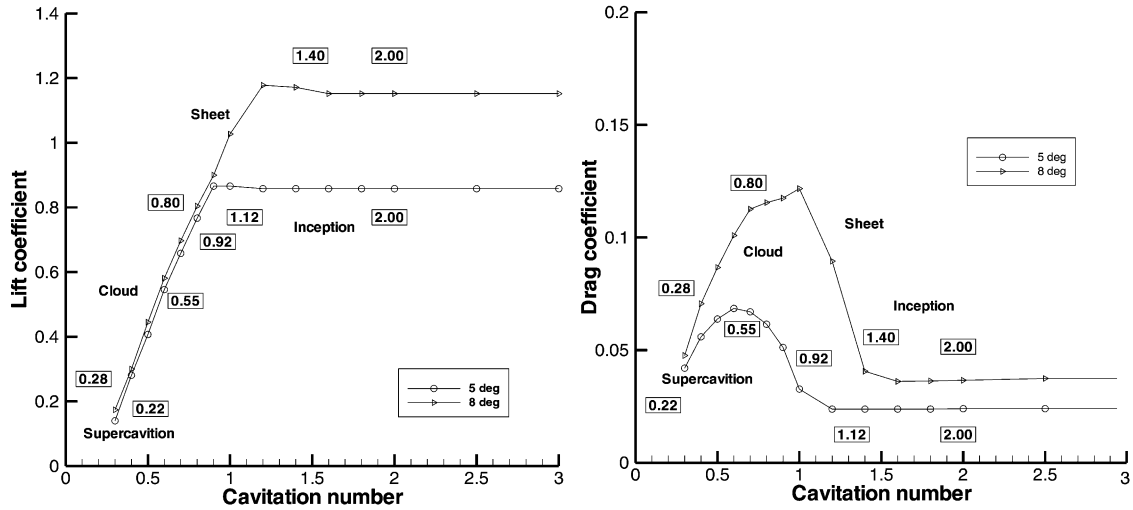


Fig. 16. Summary of the lift and drag coefficients over the entire cavitating regime, from incipient cavitation to supercavitation.

is adopted. Although the model considered does not explicitly account for the temperature, and hence Mach number, effect, it is demonstrated by Senocak and Shyy [71,72] that the density variations, which are caused by cavitation modeling, share similar features to that of high speed flows. This aspect is distinctly different from, say, a low speed chemically reacting flow [76], where the density variation, while substantial, does not impact the characteristics of the pressure correction equation. In the low Mach number chemical reacting flows, the pressure correction equation is of a diffusive type, while in the context of the cavitating flow model, it becomes a convective–diffusive type.

In Section 3.1 the governing equations at a phase-change interface will be summarized, and then in Section 3.2, the Rayleigh–Plesset equation regarding the bubble dynamics will be presented. Section 3.3 will present a modified cavitation criterion based on the cavitation parameter and stress balance. The Reynolds-averaged governing equations for mass, momentum and turbulent quantities, and the main features of transport equation based cavitation model are presented in Section 3.4. Selected solutions will be presented in Section 3.5 to assess the capability of the current state of computational modeling.

### 3.1. Dynamics and governing equations at a phase-change interface

In Fig. 17 an interface separating a liquid and its vapor during evaporation process is shown schematically. At the interface the system must satisfy the conservation of mass, momentum and energy. Follow-

ing the formulation presented in Shyy [75] and Carey [77], the velocities are with respect to a stationary observer. The normal velocity of the liquid moving toward the interface is represented by  $V_{l,n}$ , and the normal velocity of the vapor moving away from the interface is represented by  $V_{v,n}$ . The interface has a normal velocity of  $V_{I,n}$ .

#### 3.1.1. Conservation of mass

The mass flow into the interface must be equal to the mass flow out:

$$\rho_l(V_{l,n} - V_{I,n}) = \rho_v(V_{v,n} - V_{I,n}), \quad (2)$$

where  $\rho_l$  and  $\rho_v$  are the density of the liquid and vapor phases respectively.

#### 3.1.2. Conservation of momentum in the normal direction

$$P_v - P_l = \gamma \left( \frac{1}{R_1} + \frac{1}{R_2} \right) + 2\mu_v \frac{\partial V_{v,n}}{\partial n} - 2\mu_l \frac{\partial V_{l,n}}{\partial n} + \rho_l(V_{l,n} - V_{I,n})^2 - \rho_v(V_{v,n} - V_{I,n})^2 \quad (3)$$

$\gamma$  is the surface tension,  $R_1$ ,  $R_2$  are the principal radii of curvature of the interface measured positive on the vapor side of the interface,  $P_v$  and  $P_l$  are the pressures of the vapor and liquid phases respectively.  $\mu_v$  and  $\mu_l$  represent absolute viscosities of the vapor and the liquid phases respectively.

#### 3.1.3. Conservation of momentum in the tangential direction

It is assumed that the interface is very thin and surface tension is constant. Also tangential velocities of each

phase at the interface are equal due to the no-slip condition.

$$\mu_l \left( \frac{\partial V_{l,n}}{\partial s} + \frac{\partial V_{l,s}}{\partial n} \right) = \mu_v \left( \frac{\partial V_{v,n}}{\partial s} + \frac{\partial V_{v,s}}{\partial n} \right). \quad (4)$$

### 3.2. Derivation of Rayleigh–Plesset equation

Rayleigh [63] presents a mathematical analysis of the growth and collapse of a spherical cavity. The equation in its most general form is known as the Rayleigh–Plesset equation. Due to its unique nature of being the main analytical form describing the cavitation dynamics, in this section, we recount the derivation of Rayleigh–Plesset equation following Knapp et al. [2] and Brennen [4]. Consider a spherical bubble of radius  $R(t)$  in an infinite domain of liquid then the Rayleigh–Plesset equation including the effect of viscosity and surface tension reads the following [4]:

$$\frac{P_B(t) - P_\infty(t)}{\rho_l} = R \frac{d^2 R}{dt^2} + \frac{3}{2} \left( \frac{dR}{dt} \right)^2 + \frac{4v_l dR}{R dt} + \frac{2\gamma}{\rho_l R}. \quad (5)$$

In the above equation  $R$  is the radius of the spherical cavity,  $\rho_l$  is the liquid density,  $v_l$  is liquid kinematic viscosity,  $P_B(t)$  is the pressure inside the cavity,  $P_\infty(t)$  is the pressure of the free stream and  $\gamma$  is the surface tension.

The Rayleigh–Plesset equation offers a nonlinear description of the bubble dynamics in a transient manner. While assuming spherical symmetry, it accounts for viscosity, surface tension, and inertia effects to relate the pressure variations across the bubble interface and the bubble radius. Computational models have been developed to simulate the bubble dynamics and its implication in shock formation and acoustics [78]. However, it is a global model in the sense that the dynamic balance among the physical mechanisms is maintained for the entire bubble; neither local transport of mass and momentum around the liquid–vapor interface, nor the non-spherical geometry is considered. To offer a detailed predictive capability for attached, turbulent cavitating flows, alternative models accounting for local mass and momentum transfer across the interface need to be considered.

### 3.3. Cavitation inception and cavitation parameter

Commonly used criterion for cavitation inception is based on a static approach and states that the cavities will occur when the hydrodynamic pressure drops below the vapor pressure of the liquid at the free stream temperature. This can be formulated as:

$$P < P_v. \quad (6)$$

Joseph [79] proposes a new criterion, which can account for anisotropic flow structure. The criterion is formulated in terms of the principal stresses occurring in a moving fluid rather than the pressure in a static fluid used commonly. The formulation is based on the idea that the liquid will rupture in the direction of maximum tension and it is stated that this can lead to cavity formation under different conditions. For a Newtonian fluid the criterion can be written as follows:

$$\frac{\partial u}{\partial x} > \frac{P - \bar{P}_v}{2\mu}, \quad (7)$$

where  $P_v$  is an empirical criterion that replaces  $P_v$  to take into account the impurities for practical applications. Since the dynamics of the flow is taken into consideration cavity formation can occur under different conditions than Eq. (6). No study has been found utilizing this criterion.

It should be noted that cavitation parameter  $\sigma$  is not strictly a parameter of similitude for cavitating flows. It is a necessary but not a sufficient condition. It is known that nuclei present in free stream flow have an impact on the two-phase flow structure.

### 3.4. Governing equations and transport equation based cavitation modeling

The set of governing equations consists of the conservative form of the Reynolds-averaged N–S equations, plus a volume fraction transport equation to account for the cavitation dynamics. The equations, written in the Cartesian coordinates for the ease of presentation, are presented below.

$$\frac{\partial \rho_m}{\partial t} + \frac{\partial (\rho_m u_j)}{\partial x_j} = 0, \quad (8)$$

$$\begin{aligned} \frac{\partial}{\partial t} (\rho_m u_i) + \frac{\partial}{\partial x_j} (\rho_m u_i u_j) = \\ - \frac{\partial p}{\partial x_i} + \frac{\partial}{\partial x_j} \left[ (\mu + \mu_t) \left( \frac{\partial u_i}{\partial x_j} + \frac{\partial u_j}{\partial x_i} \right) \right], \end{aligned} \quad (9)$$

$$\frac{\partial \alpha_l}{\partial t} + \frac{\partial}{\partial x_j} (\alpha_l u_j) = (\dot{m}^- + \dot{m}^+). \quad (10)$$

The mixture density and the turbulent viscosity are defined, respectively, as follows:

$$\rho_m = \rho_l \alpha_l + \rho_v (1 - \alpha_l) \quad \mu_t = \frac{\rho_m C_\mu k^2}{\varepsilon}. \quad (11)$$

Physically, the cavitation dynamics is governed by the thermodynamics and the kinetics of the phase change dynamics occurring in the system. These processes are modeled through  $\dot{m}^-$  and  $\dot{m}^+$  terms in Eq. (10), which represents evaporation and condensation of the phases, respectively, and results in a variable density field. Surface tension and buoyancy effects are neglected considering the typical situation that Weber and Froude

numbers are large. The particular form of these phase transformation rates are adopted from Kunz et al. [67,68]. The values of the empirical constants  $C_{\text{dest}}$  and  $C_{\text{prod}}$  for each simulation are presented along with corresponding figures and they are different than the values reported in other studies using the same cavitation model. The sensitivity of the simulations to these constants is also studied. The source terms commonly adopted are given below:

$$\begin{aligned}\dot{m}^- &= \frac{C_{\text{dest}} \rho_v \alpha_l \text{MIN}[0, p - p_v]}{\rho_l \left( \frac{1}{2} \rho_l U_\infty^2 \right) t_\infty} \dot{m}^+ \\ \dot{m}^+ &= \frac{C_{\text{prod}} \rho_v \alpha_l^2 (1 - \alpha_l)}{\rho_l t_\infty}.\end{aligned}\quad (12)$$

The time scale in the equation is defined as the ratio of the characteristic length scale to the reference velocity scale ( $l/U$ ).

The transport equation model offers a useful computational framework because it does not assume any particular geometry, and allows two-way phase change between liquid and vapor. Furthermore, intrinsic to the model is that the coexistence of the vapor–liquid mixture at a given location is allowed. Such a scenario can result from either insufficient resolution of the grid and/or numerical procedures, or true physics. In either event, it enables one to examine the attached cavity dynamics in the context of turbulence and phase boundary interactions. For example, the nominal density ratio ( $\rho_l/\rho_v$ ) is the ratio between thermodynamic values of density of

liquid and vapor phases at the corresponding flow condition; a value of 1000 is taken in computations performed by Kunz et al. [67,68] and Senocak and Shyy [71,72]. As will be illustrated later, the mass transfer model often results in solutions with a density field much higher than that of the pure vapor, thus indicating the importance of density distributions in the assessment of the results.

### 3.4.1. Turbulence modeling

For the turbulence closure, the original  $k-\varepsilon$  turbulence model with wall functions is a popular choice [80,81].

$$\begin{aligned}\frac{\partial \rho_m k}{\partial t} + \frac{\partial \rho_m u_j k}{\partial x_j} \\ = P - \rho_m \varepsilon + \frac{\partial[(\mu + \mu_t/\sigma_k)\partial k/\partial x_j]}{\partial x_j},\end{aligned}\quad (13)$$

$$\begin{aligned}\frac{\partial \rho_m \varepsilon}{\partial t} + \frac{\partial \rho_m u_j \varepsilon}{\partial x_j} = C_{\varepsilon 1} \frac{\varepsilon}{k} P - C_{\varepsilon 2} \rho_m \frac{\varepsilon^2}{k} \\ + \frac{\partial[(\mu + \mu_t/\sigma_\varepsilon)\partial \varepsilon/\partial x_j]}{\partial x_j}.\end{aligned}\quad (14)$$

The turbulent production, Reynolds stress tensor terms, and the Boussinesq eddy viscosity concept are defined as follows.

$$P = \tau_{ij} \frac{\partial u_i}{\partial x_j} \quad \tau_{ij} = -\overline{\rho u'_i u'_j}.\quad (15)$$

In the above equations  $C_{\varepsilon 1}$ ,  $C_{\varepsilon 2}$ ,  $\sigma_k$ ,  $\sigma_\varepsilon$  are empirical constants. For certain types of flows, such as flows with recirculation, rotation and large streamline curvatures, equilibrium between the turbulent production and dissipation is not maintained, these constants should be modified because they are originally determined based on the equilibrium conditions. The coefficients  $C_{\varepsilon 1}$ ,  $C_{\varepsilon 2}$  regulate the production and dissipation in the  $\varepsilon$  equation, respectively. The empirical constants used in these models are tabulated in Table 4. Further information about these models and applications for different test cases are given in Shyy et al. [82].

Eddy viscosity closures, such as the  $k-\varepsilon$  and the  $k-\omega$  models, have been commonly adopted for computing turbulent flows in practical applications since they are relatively robust and computationally inexpensive. However, it is well established that the eddy viscosity models (EVMs) do not correctly reflect the sensitivity of turbulent stresses to streamline curvature, body forces,

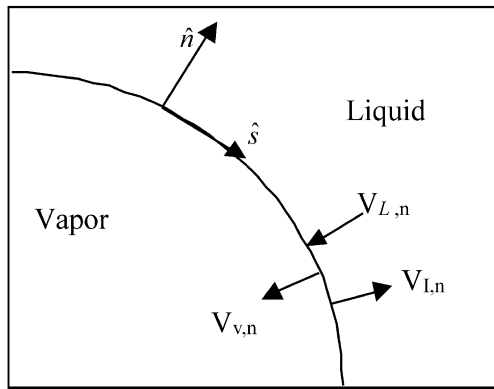


Fig. 17. Schematic of a liquid-vapor interface.

Table 4  
Empirical constants used in  $k-\varepsilon$  turbulence model

Model	$C_\mu$	$C_{\varepsilon 1}$	$C_{\varepsilon 2}$	$\sigma_k$	$\sigma_\varepsilon$
Original $k-\varepsilon$	0.09	1.44	1.92	1.0	1.3
Non-equilibrium $k-\varepsilon$	0.09	$1.15 + 0.25(P/\varepsilon)$	$1.45 + 0.45(P/\varepsilon)$	0.8927	1.15

strong transport effects, etc. Reynolds stress models (RSMs)—also known as second-moment closure models—provide an alternative which, although still need modeling for certain turbulence correlations, eliminate or reduce the above deficiencies inherent to eddy viscosity models.

The main questions, which need to be addressed, include:

1. The non-equilibrium effects as reflected in the establishment of the model parameters as well as mathematical expressions of the various physical mechanisms.
2. The nonlinear behavior of the pressure–strain correlation and the related wall effects.
3. Low-Reynolds number effects as the turbulent scales become smaller during the mixing process as well as when approaching solid boundaries.
4. Time-dependency aspects of the non-stationary turbulent flows, often observed in flows with large streamline curvatures or flow separation.
5. Compressibility effects to model supercavitating flows as well as to account for much reduced values of speed of sound in vapor–liquid water mixtures.

Based on the existing experiences with the  $k-\varepsilon$  model (see, e.g., Shyy et al. [82]), the two coefficients regulating the magnitude of the production and dissipation in the  $\varepsilon$  equation ( $C_{\varepsilon 1}$  and  $C_{\varepsilon 2}$ ) are usually not constants. The coefficients  $C_{\varepsilon 1}$  and  $C_{\varepsilon 2}$  are determined largely based on the equilibrium condition, in which case the production and dissipation of  $k$  balance each other and convective/diffusive effects are negligible. However, for flows with swirl, adverse pressure gradient, recirculation, and large streamline curvature, flow equilibrium does not exist.

Modifications have been proposed to the original  $k-\varepsilon$  two-equation model to account for the effect of recirculation and large mean strain rate [83–85]. The experiences gained there can also be useful in the present context because the  $\varepsilon$ -equation is also needed in the RSM approach. It seems useful to add a time scale in the  $\varepsilon$ -equation by introducing a functional form for  $C_{\varepsilon 1}$ , to account for non-equilibrium between production and dissipation. As reviewed by Shyy et al. [82], this modification results in the non-equilibrium model. This model has been tested in compressible and incompressible recirculating flows with improved performance [82]. A further modification can be made by allowing a similar variation for the coefficient  $C_{\varepsilon 2}$ . The motivation for allowing to vary is to allow to respond to the ratio of the production and dissipation of the turbulent kinetic energy.

The effect of compressibility on the turbulence structure is an important but difficult issue in turbulence modeling. Modeling issues in both the production and

dissipation of turbulent kinetic energy need to be addressed to account for density and temperature variations. Several issues in this regard are discussed in Shyy et al. [82] and Shyy and Krishnamurty [86].

- (a) A representation for the turbulent mass flux term, using experimentally validated assumptions.
- (b) A representation for the enthalpic production, which tends to be an important term when considering flows involving strong expansions and compressions.
- (c) A representation for the effect of the baroclinic term on the dissipation rate of TKE.

In addition to the eddy-viscosity models, higher moment closures have been investigated extensively in recent years. The Reynolds stress models use the exact equations for the transport of Reynolds stresses, which are obtained by taking velocity-weighted moments of the N–S equations. Though the first such model was proposed in 1951, it is only in the last decade or so that RSMs have been increasingly employed for practical turbulent flows involving recirculation and complex geometries [83,87–89]. The hope with second-moment closure is that uncertainties in modeling the higher-order correlations will be smoothed out and diminished in the process of integration to the lower-order, thus allowing a broader class of flows to be modeled. However, in practice, the RSM has not become a truly robust alternative for complex turbulent flows.

In addition to the above-mentioned approaches, there are also proposals based on nonlinear eddy viscosity and algebraic stress models [90], very large eddy simulation [91], and large eddy simulation [92]. Suffice it to say that turbulence modeling for cavitating flow is a highly uncertain area because to date, insufficient efforts have been made to evaluate the various models against well-established experimental evidences. Clearly, substantial efforts will be required before one can apply with confidence any turbulence models to cavitating flows.

### 3.4.2. Pressure-based computational techniques

In the pressure-based algorithm, the pressure correction equation has been revised to achieve successful solutions for highly compressible flows [75,93–95]. For highly compressible flows, density needs to be corrected to account for the strong pressure–density dependency. For such a formulation the flux terms in the continuity equation can be expressed as follows:

$$\begin{aligned}\rho U &= (\rho^* + \rho')(U^* + U') \\ &= \rho^* U^* + \rho^* U' + \rho' U^* + \rho' U',\end{aligned}\quad (16)$$

where  $\rho U$  term is the mass flux entering the control volume. Starred variables represent the guessed value

and primed variables represent correction terms. In the incompressible formulation, only the first two terms on the right hand side exist. The last two terms appear for the compressible formulation. The second term in the above equation results in a diffusive character in the pressure-correction equation, while the third term results in a convective character. As discussed in Shyy [75], their relative importance depends on the local Mach number; for low Mach number flows, only the first two terms prevail, while for high Mach number the third and fourth terms become important. The Mach number dependency can be shown through the equation of state. The fourth term is a nonlinear correction term and it can either be neglected or included in the source term to stabilize the computation in early iterations.

In the cavitation model a convection equation with pressure dependent source terms, Eq. (10), is solved to determine the density field. Because of the coupling between pressure and density, the pressure correction equation needs to be reformulated even though the Mach number effect is not explicitly addressed in the model. Due to Eqs. (10) and (12), once the cavitation model is implemented into a pressure-based algorithm, the pressure correction equation exhibits a convective-diffusive nature in cavitating regions and purely diffusive nature in the liquid phase. Senocak and Shyy [71] introduce the following relation between density and pressure corrections to establish the pressure–velocity–density coupling.

$$\rho' = C(1 - \alpha_l)P', \quad (17)$$

where  $C$  is an arbitrary constant. It should be emphasized that the choice of this constant does not affect the final converged solution because of the nature of the *pressure correction* equation.

Similar to the interpolation of density at the cell face in compressible flow computations [75,93], Senocak and Shyy [71] also utilize an upwinded density interpolation at the cell face. The criterion for upwinding is based on the value of liquid volume fraction; that is, wherever  $\alpha_l$  is less than 1.0, the cell-faced density value is estimated based on an upwinded formula. This treatment significantly improves the convergence level and has a stabilizing effect in the vicinity of sharp density gradients. As demonstrated in Fig. 18, the residuals resulting from momentum, mass continuity and volume fraction transport equations can approach much lower levels than the original pressure correction algorithm for constant property flows and without upwinded interpolation for density. It is noted that the residuals are defined as the absolute values of the imbalance of the individual equations summed over the entire number of computational cells, normalized by the total flux of the given variable, at the inlet of the computational domain.

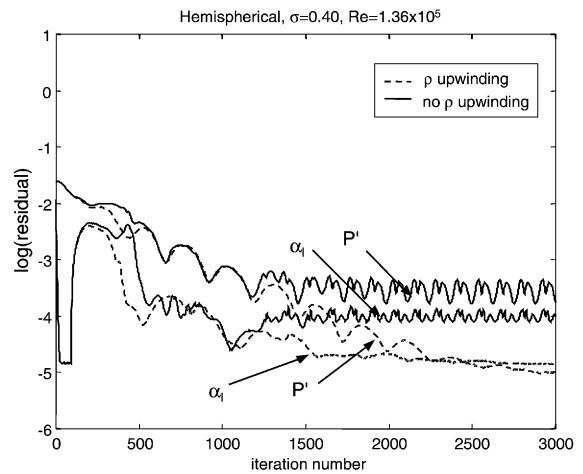


Fig. 18. Improvement in convergence level due to density upwinding. Hemispherical object at  $\sigma = 0.40$ .

### 3.4.3. Density-based computational techniques

The density-based technique has been applied extensively by Kunz, Lindau and coworkers [43,67,68,96] to cavitating flow problems. Their approach, originally developed by Taylor et al. [97] and Whitfield and Taylor [98], employs the artificial compressibility method originally proposed by Chorin [99], and later refined by others, including Merkle et al. [66] and Venkateswaran et al. [70], to improve the treatment of preconditioning so that the procedure is efficient and robust. The outcome is an implicit solver with an all-speed preconditioned differential model. These authors have applied the computational technique for simultaneous simulation of incompressible through supersonic multi-phase flows.

### 3.4.4. Modeling of multi-scale and interfacial dynamics

The above review of the pressure- and density-based solution techniques is concerned with the handling of the set of partial differential equations which couples the conservation of mass and momentum, and turbulent and cavitation models. In addition, based on the experimental evidences, it seems clear that cavitating flows have several unique computational challenges, including interfacial conditions between liquid and vapor phases, thermodynamic models for both slow and fast cavity characteristics, large disparity in speed and turbulence modeling. Furthermore, downstream of the cavitating domain, the vapor phase may break into many bubbles instead of one clearly defined entity. Accordingly, a statistical approach will be useful for handling the many-bubble case. In the following, we present selected research thrust related to computation and physical modeling.

**3.4.4.1. Multi-level cavitating flow model.** Regarding the cavitation model, the proposed effort consists of a two-pronged plan: first, develop an accurate and robust CFD tool for analyzing overall flow field and for tracking liquid–vapor interface, and second, develop a multi-scale model. The multi-scale model can utilize a microscopic model to simulate individual bubbles in limited domain size, with the goal of generating information needed to construct an information base, based on probability function, to supply volume-averaged quantities in the macroscopic model.

Specifically, the multi-scale modeling technique groups the microscale effects due to individual bubbles via a filtering procedure in the macroscopic equations. The microscale terms, which contribute to the averaged effect viewed from the length and time scales appropriate to the macroscopic transport equations, are modeled based on the data base generated from the ensembles of simulations conducted at the microscopic scale. The local conditions resulting from the solutions of the equations written at the macroscopic scale, on the other hand, can be used as the boundary conditions for the microscopic analyses. From a macroscopic (coarse-grained) view, this model treats the cavity flow field phenomenologically as a compressible viscous fluid whose density varies greatly. Thus the model treats the inside and outside of the cavitation as a single continuum. In a microscopic view, it treats cavitation structurally as a bubble clusters. According to this phenomenological modeling, contour lines of the void fraction (volume fraction of cavities) express the shape of cavity. In short, at the macroscopic level, no detailed knowledge of the detailed characteristics of particular cavitating bubbles are known, while in the microscopic level the overall flow field is not accounted for except in the immediate vicinity of each bubble. Of course, the information of this localized flow field is deduced from the macroscopic simulation. Such an approach has been advocated in Shyy et al. [100].

Such a two-way coupling can proceed until both scales have yielded definitive solutions. Construction of a single numerical grid to capture the flow on the global (macro) scale and all of the local (micro) scales would not only be difficult, but prohibitive in terms of usefulness in the design process.

As a first step toward developing such a multi-scale model, a locally homogenized model (LHM) can be useful. Bubble number density and probability distribution of the radius of cavitating bubbles are assessed locally. The LHM gives the local void fraction by coupling the bubble density and averaged effects by accounting for the probability distribution of bubble radius. Then the interfacial condition surrounding a cavitating bubble needs to be developed.

The fundamental tenet behind the design of the multiple-scale approach is to separate the solutions of the global and local scales. Since the two levels must communicate in some manner in order to produce a meaningful result overall, some form of modeling to connect the two levels is required.

**3.4.4.2. Interface tracking algorithm.** With the presence of liquid–vapor interface, both normal and shear forces, involving pressure, viscosity, and velocity gradients, and mass transfer rate play important roles. Together with surface tension, the interface shape is determined. Within both fluid and vapor phases, the field equations need to be solved with the location of their boundary being determined simultaneously. From a continuum mechanics viewpoint, the phase interface is a discontinuity in the continuum field. Within the context of finite grid resolution, the discontinuity needs to be accurately tracked in time and in space.

In moving boundary problems, not only are the transport of momentum, mass, and phase fraction coupled, but also the formation, evolution, and dynamics of the interface play major roles in defining the behavior of the system. Apart from the inherent nonlinearity of these diverse phenomena, the interfacial deformation in itself can be a highly complicated and analytically intractable feature. Frequently, physical phenomena involve interfaces that, as a result of instabilities or external impulses, undergo severe deformations, such as dilatation, compression, fragmentation, and collision. Numerous techniques exist for tracking arbitrarily shaped interfaces, each with its own strengths and weaknesses [101]. These techniques may be classified under two main categories: (a) surface tracking or predominantly Lagrangian methods and (b) volume tracking or Eulerian methods.

In the Lagrangian methods, the grid is configured to conform to the shape of the interface, and thus it adapts continually to it. The Eulerian methods usually employ a fixed grid formulation, and the interface between the two phases is not explicitly tracked but is reconstructed from the properties of appropriate field variables, such as phase fractions. Extensive efforts have also been made to combine the performance merits of the Eulerian and Lagrangian approaches, in which, typically, the interfaces are described by means of markers indexed sequentially and separated into objects. There is no restriction on the number of objects or on the end conditions that can be imposed on these curves. The objects can be open or closed. Furthermore, they can be fixed or moving. They can enclose different phases or materials with different properties. Once the interface description is obtained in terms of markers and their positions, the shape characteristics such as normals and curvatures can be extracted.

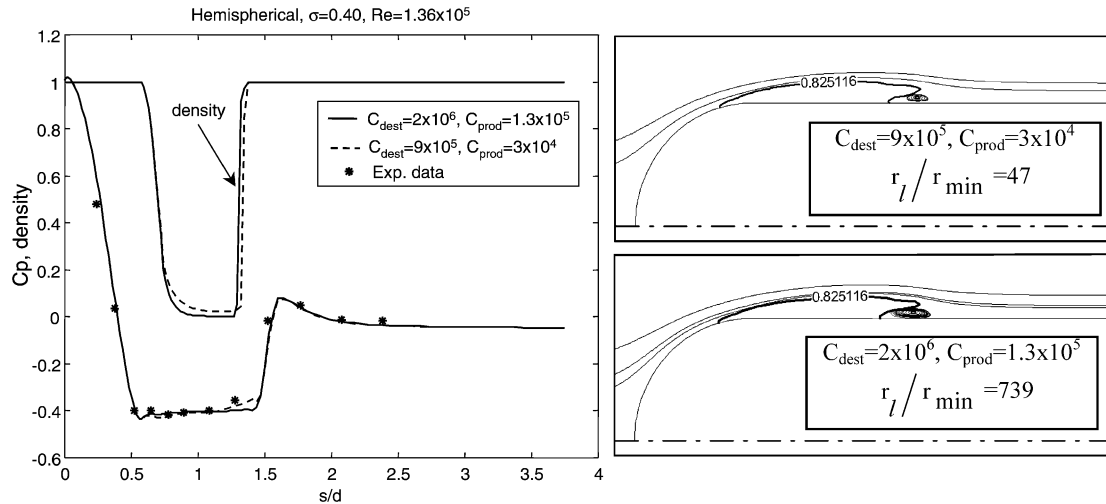


Fig. 19. Sensitivity of modeling parameters for the hemispherical object at  $\sigma = 0.40$  ( $\rho_l/\rho_v = 1000$ ).

### 3.5. Assessment between computation and experiment

Senocak and Shyy [71,72] have presented solutions based on two different axisymmetric geometries and an airfoil geometry to investigate numerical and physical issues involved in cavitation modeling. Both geometries considered have a cylindrical after-body and they are referred to according to the shape of their headforms, specifically, hemispherical or blunt. The results include steady-state computations of non-cavitating and cavitating flows at a Reynolds number of  $1.36 \times 10^5$ . Results for cylindrical geometries from the computations of Senocak and Shyy [71] are compared with experimental results of Rouse and McNown [102] in which pressure coefficients are reported. Since the experimental information does not report time dependency, the steady-state model is adopted in their computations. From the physical point of view, the steady-state assumption is sensible for sheet cavitation, which has a quasi-steady behavior, with most of the unsteadiness localized in the rear closure region [2]. However, as have been discussed, unsteady characteristics are typical for cases beyond sheet cavitation.

First, in Fig. 19, the sensitivity of the solutions to parameters of the cavitation model is studied in the context of the hemispherical cylinder. It can be seen that even increasing these parameter by an order of magnitude has little effect on the pressure coefficient predictions. However, the computed density ratio is noticeably different between these model parameters. Clearly, the computed density ratios can be controlled through adjustment of the model parameters to yield very different solutions while pressure predictions remain little unaffected.

Fig. 20 demonstrates the predictive capability of the model at cavitation numbers of 0.40 and 0.30 through comparison with experimental data of Rouse and McNown [102]. Identical model parameters are adopted for both cavitation numbers. The pressure distribution corresponding to the non-cavitating condition is also plotted for comparison. The computational method developed by Senocak and Shyy [71] performs well for both cavitating and non-cavitating conditions. The corresponding cavity profiles, streamlines and computed density ratios are also presented in Fig. 20. The computed cavity profiles are in the form of pinched pockets with re-entrant jets in the closure region. With a lower cavitation number ( $\sigma = 0.30$ ), the cavity, as expected, becomes larger than that with a cavitation number ( $\sigma = 0.40$ ). The re-entrant jet is also stronger suggesting that at lower cavitation numbers the re-entrant jet can easily perturb the cavity, possibly leading to shedding of bubbles. The computed density ratio is higher for  $\sigma = 0.30$ , because the source terms are effective on more grid points. The cavity detachment point remains fixed in both of the simulations, which is also in agreement with experimental data. In Fig. 21 the effect of cavitation on wall shear stress distribution is studied. By comparing the skin friction coefficient of both non-cavitating and cavitating conditions, one can see that the existence of cavitation not only alters the flow structure inside the cavity but it also affects the downstream flow. The turbulent viscosity distributions indicate that the re-entrant jet gets more dissipative as the cavitation number is lowered, which suggests that the viscous effects can play an important role on the overall cavity behavior such as the reattachment location.



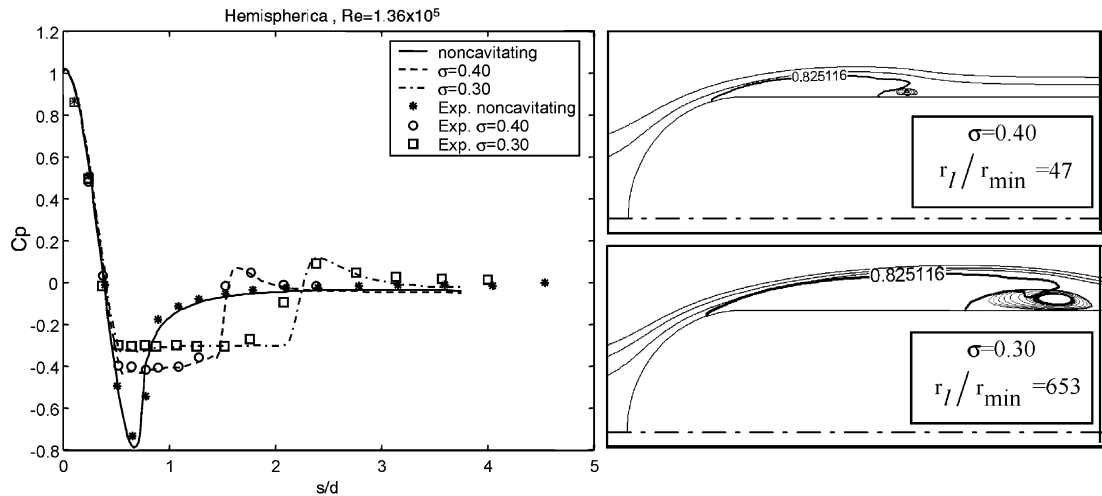


Fig. 20. Comparison of pressure coefficient distributions for hemispherical object under *noncavitating* and *cavitating* conditions ( $C_{dest} = 9 \times 10^5$ ,  $C_{prod} = 3 \times 10^4$ ,  $\rho_l/\rho_v = 1000$ ). Experimental data is from [102].

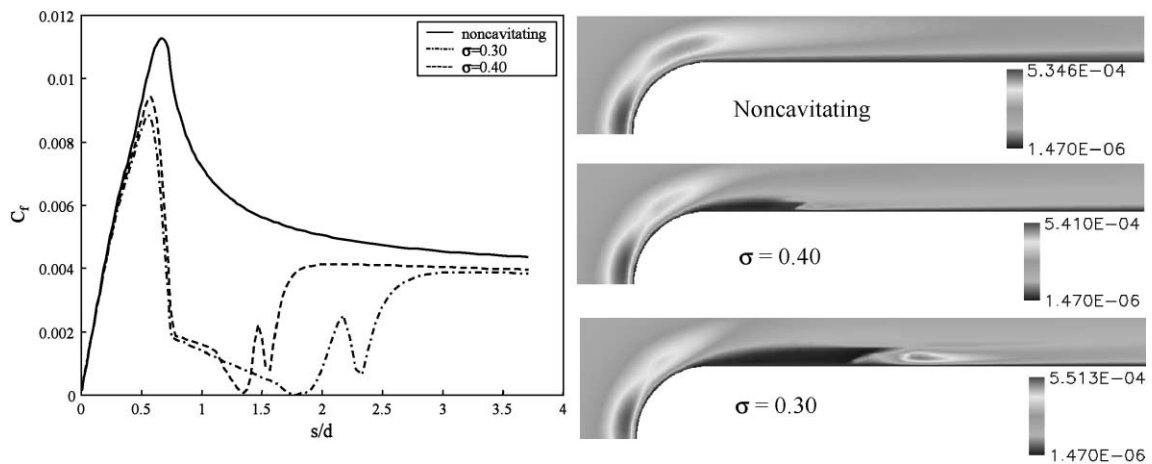


Fig. 21. Effect of cavitation on wall shear stress. Corresponding turbulent viscosity distributions are on the right part of the figure.

Assessment has also been made in regard to the blunt cylindrical object. For this particular object, Rouse and McNown [102] have provided the pressure coefficient distribution along the body, and Katz [8] has reported flow reattachment locations. In view of the potential deficiencies associated with the original  $k-\epsilon$  turbulence model [80], for complex flows, a non-equilibrium version of the  $k-\epsilon$  model [82] is studied in addition to the original  $k-\epsilon$  model [80]. Both non-cavitating and cavitating conditions have been studied to investigate the turbulence modeling issue. Fig. 22 shows the pressure coefficient profile for the non-cavitating condition. The original  $k-\epsilon$  model fails to match the

experimental data in the vicinity of the sharp corner where large strains and streamline curvatures are expected to occur. On the other hand, the non-equilibrium  $k-\epsilon$  model performs better to capture the pressure coefficient distribution. Fig. 23 shows the normalized  $u$ -velocity distribution along the body that is extracted from the first computational nodes away from the solid boundary. The point where velocity changes sign is the reattachment point. One can see that there are considerable differences in predictions of reattachment locations and associated velocity profiles between two turbulence models. It is observed that the reattachment point location, predicted with the

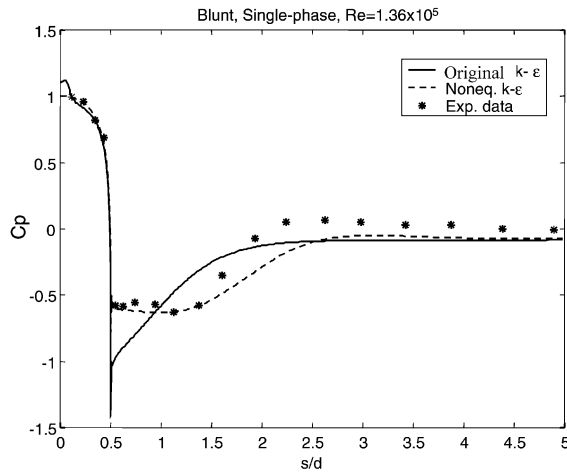


Fig. 22. Impact of turbulence modeling on predictions of pressure coefficient distribution for non-cavitating conditions. Experimental data is from Rouse and McNown [102].

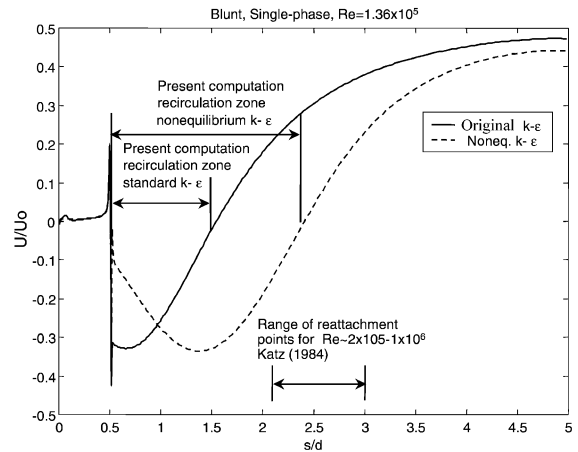


Fig. 23. Effect of turbulence model on separation zones for non-cavitating conditions. Experimental data is from Katz [8].

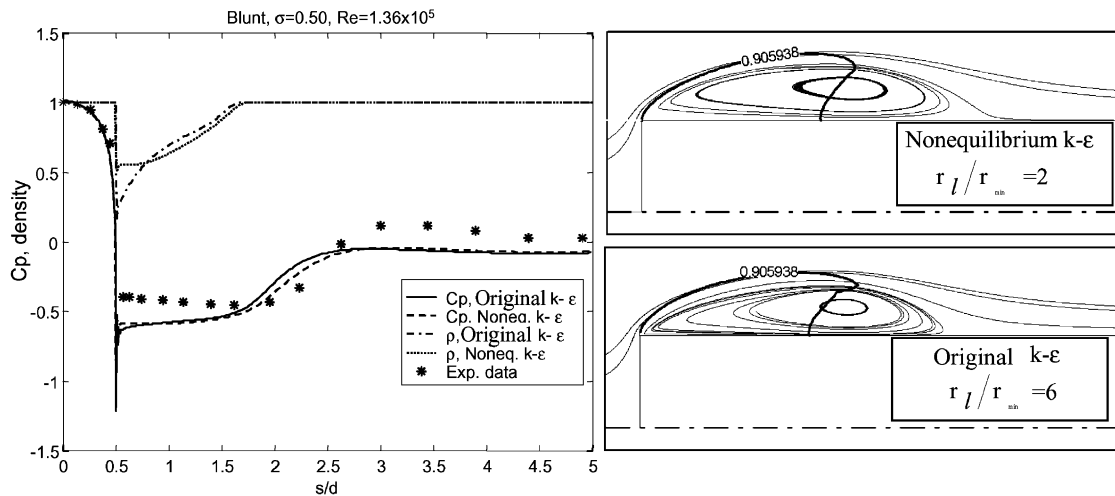


Fig. 24. Impact of turbulence modeling on predictions of pressure coefficient and density distribution ( $\sigma = 0.50$ ,  $C_{dest} = 1.8 \times 10^4$ ,  $C_{prod} = 6 \times 10^3$ ,  $\rho_l/\rho_v = 1000$ ). Experimental data is from Rouse and McNown [102].

non-equilibrium  $k-\epsilon$  model, is consistent with the experimental data of Katz [8] even though the Reynolds number range is not the same. It should be noted that Katz [8] has not observed a strong correlation between reattachment location and Reynolds number for this range. Overall, the non-equilibrium  $k-\epsilon$  model performs better, compared to the original  $k-\epsilon$  model, in capturing the pressure coefficient distribution and the extent of separation zones. Based on this observation, the non-equilibrium  $k-\epsilon$  model is included in the study of cavitating flows over blunt objects.

Fig. 24 shows the pressure coefficients and density profiles along the blunt object at a cavitation number of 0.50. Cavity profiles and streamlines are also included in Fig. 24. Computed pressure profiles qualitatively follow the experimentally observed trend. Unlike non-cavitating flow computations, both turbulence models considered produce similar results. Fig. 25 illustrates the normalized  $u$ -velocity profile along the surface. The difference in predicted reattachment location is also less significant between the two turbulence models. Furthermore, both solutions exhibit

rather modest density ratios across the cavity interface, suggesting that inside the cavity the flow exhibits liquid–vapor bubbly structures. The discrepancy between computational and experimental results may be caused by the steady-state computations. Stinebring et al. [34] employ high-speed visualization and report that cavities formed around blunt objects are highly unsteady and bubbling phenomenon is typically observed.

In Fig. 26, the turbulent kinetic energy  $k$  and turbulent dissipation rate  $\varepsilon$ , resulting from the original

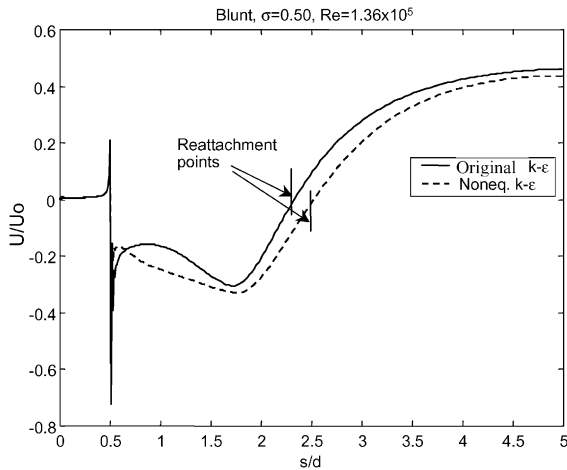


Fig. 25. Comparison of  $u$ -velocity along the surface obtained from different turbulence models ( $\sigma = 0.50$ ,  $C_{dest} = 1.8 \times 10^4$ ,  $C_{prod} = 6 \times 10^3$ ,  $\rho_l/\rho_v = 1000$ ).

and non-equilibrium  $k-\varepsilon$  turbulence models, are compared. In both cases, the turbulent variables are of higher levels following the shear layer surrounding the cavity; however, the detailed distributions are different. The non-equilibrium model yields more substantial presence in both  $k$  and  $\varepsilon$ . Together, they are responsible for a somewhat longer recirculating zone, as shown in Fig. 9. Although the predictions of pressure are less sensitive to turbulence modeling, other quantities such as wall shear stress and velocity profiles can be more affected by it.

Fig. 27 presents the pressure distribution along with the cavity shape. The angle of attack is  $1^\circ$  and the cavity occurs at mid chord with a corresponding cavitation number of 0.42. These conditions and the overall behavior of the cavity are consistent with the experimental study of Shen and Dimotakis [55] in which the NACA66MOD airfoil is investigated. The corresponding vapor pressure is recovered inside the cavity region, consistent with results of the hemispherical object. Unlike the hemispherical object, no re-entrant jet is observed in this case, possibly because the cavity is in the form of a thin layer.

#### 4. Summary and conclusions

Attached, turbulent cavitating flows of different cavitation regimes around solid objects are reviewed from experimental and computational viewpoints. Depending on the cavitation number and the incidence angle, different flow structures can be identified. Following is a summary of the main findings:

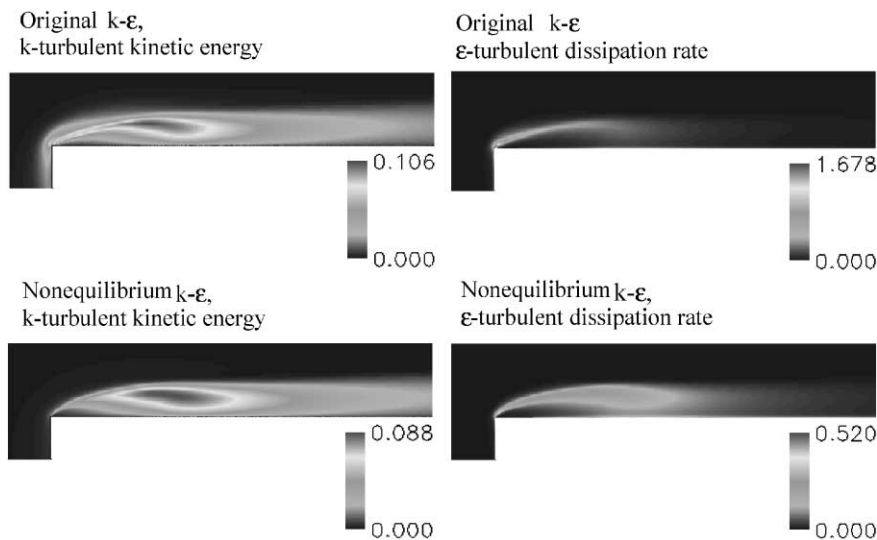


Fig. 26. Comparison of turbulence quantities obtained from different turbulence models ( $\sigma = 0.50$ ,  $C_{dest} = 1.8 \times 10^4$ ,  $C_{prod} = 6 \times 10^3$ ,  $\rho_l/\rho_v = 1000$ ).

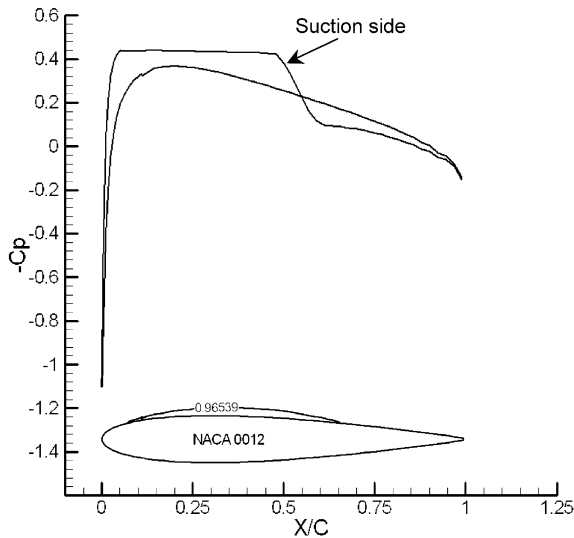


Fig. 27. Sheet cavitation on NACA 0012 airfoil at  $\sigma = 0.42$ ,  $\rho_l/\rho_{\min} = 8$  ( $C_{\text{dest}} = 9 \times 10^5$ ,  $C_{\text{prod}} = 3 \times 10^4$ ,  $\rho_l/\rho_v = 1000$ ).

In non-separating flow region of the flow around a hydrofoil, cavitation inception is related to the coherent structures in boundary layer. Cavitation bubbles are generated along with counter-rotating vortex pair, typically developing into hairpin-shaped cavitating flow structures.

In incipient cavitation, the time scales of the growth, merging, and collapse of the hairpin-shaped cavitating vortices are consistently recorded. By lowering the cavitation number, the hairpin structures expand and merge, resulting in a sheet cavity with a finger-like front. The rear portion of a sheet cavity exhibits an unsteady, wavy pattern. Further decreasing the cavitation number induces the growth of the wavy trailing edge, accompanying the downstream movement, which leads to the formation and shedding of large-scale vortex flows, resulting in cloud cavitation. The trailing edge of a sheet or cloud cavity exhibits noticeable unsteady characteristics, more so in cloud cavitation than in sheet cavitation. Associated with the large-scale vortex dynamics, a re-entrant flow is induced in the rear, near wall region of cloud cavitation.

Supercavitation is the final state of cavitation, which is caused by further lowering the cavitation number, and can be identified as a big cavity surrounding the solid surface continuously. At supercavitation, no discernible, large-scale vortical motion is observed while the overall flow remains turbulent. Inside the cavity, the velocity rapidly reduces the magnitude while exhibiting substantial scatter between different cavitation numbers and incidence angles. The lift and drag coefficients are clearly affected by the cavitating flow structure, reaching

minimum and maximum, respectively, at cloud cavitation, then turn around as supercavitation appears.

Because the cavitating flow problem involves multi-phase fluid systems with time-dependent and irregular interfaces, detailed measurement is very difficult to conduct. If adequate computational and modeling capabilities are developed, then numerical solutions can be used to guide the directions to be conducted in sensing and control areas. After validation, CFD can aid our understanding of cavitating flows, guide the implementation of the sensing system, and assess the control strategies. Noticeable progress has been made in recent years. In particular, N-S-based solution techniques have been reviewed. Various cavitation models along with the non-equilibrium effect in the context of the  $k-\varepsilon$  turbulence model have been summarized. While satisfactory predictions in wall pressure distribution can be made in various cases, aspects such as density and stress distributions exhibit higher sensitivity to modeling details.

In terms of the future directions in computational modeling, the following topics should be addressed.

- Assessment and development of interface tracking capabilities for irregularly shaped cavitation bubbles. Currently, the interface definition is less than precise and the cavitation dynamics cannot be fully captured, especially in view of the large density jump between liquid and vapor. A strong effort needs to be taken to validate the computational capability in capturing salient features of cavity such as cavity formation, location, shape, and movement.
- Improvement in the cavitation model. For example, statistical and multi-scale models can be fruitful for treating bubbly flows for finely structured cavitating flows.
- Development and refinement of two-phase all-Mach-number formulation to model two-phase compressibility and propulsion system. The disparity between convection and sound speeds in different regions can cause substantial stiffness and instability of the computational procedure.
- Various improved numerical methods, such as convection and source term treatments and unsteady effects, for improving the current cavitation algorithm. These aspects will help further improve the large variations associated with the field variables.
- Turbulence modeling to handle two-phase and compressibility effects. In particular, models capable of handling (i) substantial departure from equilibrium between production and dissipation of the turbulent kinetic energy, (ii) anisotropy between main Reynolds stress components, (iii) turbulence-enhanced mass transfer across the liquid–vapor interface should be stressed, and (iv) for high speed flows, compressibility effects.

## Acknowledgements

The work performed at the University of Florida has been supported by grants from National Science Foundation and Office of Naval Research.

## References

- [1] Batchelor GK. An introduction to fluid dynamics. New York: Cambridge University Press, 1967.
- [2] Knapp RT, Daily JW, Hammitt FG. Cavitation. New York: McGraw-Hill, 1970.
- [3] Lecoffre Y. Cavitation bubble trackers. Brookfield, VT: A. A. Balkema, 1999.
- [4] Brennen CE. Cavitation and bubble dynamics. New York: Oxford University Press, 1995.
- [5] Franc JP, Avellan F, Belahadji B, Billard JY, Briancon-Marjollet L, Frechou D, Fruman DH, Karimi A, Kueny JL, Michel JM. La cavitation. Grenoble Cedex, France: Presses Universitaires de Grenoble, 1995.
- [6] Arakeri VH, Acosta AJ. Viscous effects in the inception of cavitation on axisymmetric bodies. *J Fluids Eng* 1973;95(4):519–27.
- [7] Vijay H, Arakeri VH. Viscous effects on the position of cavitation separation from smooth bodies. *J Fluid Mech* 1973;68(4):779–99.
- [8] Katz J. Cavitation phenomena within regions of flow separation. *J Fluid Mech* 1984;140:397–436.
- [9] Wang G, Shintani M, Liu SJ, Shin BR, Ikohagi T. Cavitation characteristics around a hollow-jet valve (Observation by high-speed photographs and monitoring by vibration), *Trans. Japanese Turbomachinery Society*, 1998;26:361–8.
- [10] Katz J, O'Hern T. Cavitation in large scale shear flows. *J Fluids Eng* 1986;108(3):373–6.
- [11] Rood EP. Review-mechanisms of cavitation inception. *J Fluids Eng* 1991;113(2):163–75.
- [12] Arndt REA. Unsteady Operation due to cavitation. *Proceedings of 18th IAHR Symposium, USA*. 2000. p. 1–10.
- [13] Gopalan S, Katz J. Flow structure and modeling issues in the closure region of attached cavitation. *Phys Fluids* 2000;12(4):895–911.
- [14] Franc JP, Michel JM. Attached cavitation and the boundary layer: experimental investigation and numerical treatment. *J Fluid Mech* 1985;154:63–90.
- [15] Leger AT, Ceccio SL. Examination of the flow near the leading edge of attached cavitation. Part 1. Detachment of two-dimensional and axisymmetric cavities. *J Fluid Mech* 1998;376:61–90.
- [16] Pham TM, Larrarte F, Fruman DH. Investigation of unsteady sheet cavitation and cloud cavitation mechanisms. *J Fluids Eng* 1999;121(2):289–95.
- [17] Li CY, Ceccio SL. Interaction of single traveling bubbles with the boundary layer and attached cavitation. *J Fluid Mech* 1996;322:329–53.
- [18] Briancon-Marjollet L, Franc JP, Michel JM. Transient bubbles interacting with an attached cavity and the boundary layer. *J Fluid Mech* 1990;218:355–76.
- [19] Wang G, Liu S, Shintani M, Ikohagi T. Study on cavitation damage characteristics around a hollow-jet valve. *JSME Int J Ser B* 1999;42(4):649–58.
- [20] Furness RA, Hutton SP. Experimental and theoretical studies on two-dimensional fixed-type cavities. *J Fluids Eng* 1975;97(4):515–22.
- [21] Kubota A, Kato H, Yamauchi H, Maeda M. Unsteady structure measurement of cloud cavitation on a foil section using conditional sampling technique. *J Fluids Eng* 1989;111:204–10.
- [22] Le Q, Franc JP, Michel JM. Partial Cavities: global behavior and mean pressure distribution. *J Fluids Eng* 1993;115(2):243–8.
- [23] Kawanami Y, Kato H, Yamaguchi H, Tanimura M, Tagaya Y. Mechanism and control of cloud cavitation. *J Fluids Eng* 1997;119:788–94.
- [24] Avellan F, Dupont P, Rhyning I. Generation mechanism and dynamics of cavitation vortices downstream of a fixed leading edge cavity. *17th Symposium on Naval Hydrodynamics*, 1988. p. 317–329.
- [25] Wu YT, Wang DP. A wake model for free-streamline flow theory, Part 2. Cavity flows past obstacles of arbitrary profile. *J Fluid Mech* 1963;18:65–93.
- [26] Oba R, Ikohagi T. Supercavitating cascade analysis based on momentum theorem. *J Fluids Eng* 1973;95(1):113–21.
- [27] Furuya O, Acosta AJ. A note on the calculation of supercavitating hydrofoils with rounded noses. *J Fluids Eng* 1980;95(2):221–8.
- [28] Oba R, Ikohagi T, Yasu S. Supercavitating cavity observation by mean of laser velocimeter. *J Fluids Eng* 1980;102(4):433–40.
- [29] Ashley S. Warp drive underwater. *Sci Am* 2001:70–9.
- [30] RTO AVT/VKI special course: supercavitating flows, von Karman institute for fluid dynamics, Rhode-Saint-Genese, Belgium, 12–16 February 2001.
- [31] Michel J-M. Introduction to cavitation, supercavitation. RTO AVT/VKI special course: supercavitating flows, von Karman Institute for Fluid Dynamics, Rhode-Saint-Genese, Belgium, 12–16 February 2001.
- [32] Tulin MP. Lecture notes on supercavitating flows. Part 1, Supercavitation: An overview; Part 2, Mathematical approaches; Part 3, The history and principles of operation of supercavitating propellers.
- [33] Michel JM. Oscillations of ventilated cavities: Experimental aspects. RTO AVT/VKI special course: supercavitating flows, von Karman Institute for Fluid Dynamics, Rhode-Saint-Genese, Belgium, 12–16 February 2001.
- [34] Stinebring DR, Billet ML, Lindau JW, Kunz RF. Developed cavitation—cavity dynamics. RTO AVT/VKI Special course: supercavitating flows, von Karman Institute for Fluid Dynamics, Rhode-Saint-Genese, Belgium, 12–16 February 2001.
- [35] Kirschner IN. Results of selected experiments involving supercavitating flows. RTO AVT/VKI special course: supercavitating flows, von Karman Institute for Fluid Dynamics, Rhode-Saint-Genese, Belgium, 12–16 February 2001.
- [36] Garabedian PR. Variational methods in cavitation flow. RTO AVT/VKI special course: supercavitating

- flows, von Karman Institute for Fluid Dynamics, Rhode-Saint-Genese, Belgium, 12–16 February 2001.
- [37] Vasin AD. The principle of independence of the cavity sectors expansion (Logvinovich's principle) as the basis for investigation on cavitation flows. RTO AVT/VKI special course: supercavitating flows, von Karman Institute for Fluid Dynamics, Rhode-Saint-Genese, Belgium, 12–16 February 2001.
- [38] Fridman GM, Achkinadze AS. Review of theoretical approaches to non-linear supercavitating flows. RTO AVT/VKI special course: supercavitating flows, von Karman Institute for Fluid Dynamics, Rhode-Saint-Genese, Belgium, 12–16 February 2001.
- [39] Vasin AD. Supercavities in compressible fluid. RTO AVT/VKI special course: supercavitating flows, von Karman Institute for Fluid Dynamics, Rhode-Saint-Genese, Belgium, 12–16 February 2001.
- [40] Rozhdestvensky KV. Supercavitating flows: small perturbation theory and matched asymptotics. RTO AVT/VKI special course: supercavitating flows, von Karman Institute for Fluid Dynamics, Rhode-Saint-Genese, Belgium, 12–16 February 2001.
- [41] Kirschner IN. Numerical modeling of supercavitating flows. RTO AVT/VKI special course: supercavitating flows, von Karman Institute for Fluid Dynamics, Rhode-Saint-Genese, Belgium, 12–16 February 2001.
- [42] Semenenko VN. Artificial supercavitation: physics and calculation. RTO AVT/VKI special course: supercavitating flows, von Karman Institute for Fluid Dynamics, Rhode-Saint-Genese, Belgium, 12–16 February 2001.
- [43] Kunz RF, Lindau JW, Billet ML, Stinebring DR. Multiphase CFD modeling of developed and supercavitating flows. RTO AVT/VKI special course: supercavitating flows, von Karman Institute for Fluid Dynamics, Rhode-Saint-Genese, Belgium, 12–16 February 2001.
- [44] Savchenko YN. Supercavitating object propulsion. RTO AVT/VKI special course: supercavitating flows, von Karman Institute for Fluid Dynamics, Rhode-Saint-Genese, Belgium, 12–16 February 2001.
- [45] Achkinadze AS. Supercavitating propellers. RTO AVT/VKI special course: supercavitating flows, von Karman Institute for Fluid Dynamics, Rhode-Saint-Genese, Belgium, 12–16 February 2001.
- [46] Kinnas SA. Supercavitating hydrofoils, propellers: prediction of performance and design. RTO AVT/VKI special course: Supercavitating Flows, von Karman Institute for Fluid Dynamics, Rhode-Saint-Genese, Belgium, 12–16 February 2001.
- [47] Takenaka K. LDV Measurements of the unsteady cavitating flows around a hydrofoil. Master Thesis of Tohoku University, Japan, 1997.
- [48] Liu S, Higuchi J, Ikohagi T. Experimental study of cavity flow behavior on a 2-D hydrofoil. JSME Int J Ser B 1999;42(4):641–8.
- [49] Wang G. Study on complex flow phenomena in hydraulic machinery. Technical Report, Department of Thermal Engineering Tsinghua University, Beijing, China, May 2001.
- [50] Kim HT, Kline SJ, Reynolds WC. The production of turbulence near a smooth wall. J Fluid Mech 1971;50: 133–60.
- [51] Smith CR, Schwartz SP. Observation of streamwise rotation in the near-wall region of turbulence boundary layer. Phys Fluids 1983;26:641–55.
- [52] Kasagi N, Hirata M, Nishino K. Streamwise pseudo-vortical structures and associated vorticity in the near-wall region of a wall-bounded turbulence shear flow. Exp Fluids 1986;4:309–17.
- [53] Luchik TS, Tiederman WG. Timescale and structure of ejections and bursts in turbulent channel flows. J Fluid Mech 1987;174:529–52.
- [54] Kubota A, Kato H, Yamaguchi H. A new modelling of cavitating flows: a numerical study of unsteady cavitation on a hydrofoil section. J Fluid Mech 1992;240:59–96.
- [55] Shen Y, Dimotakis P. The influence of surface cavitation on hydrodynamic forces. Proceedings of the 22nd ATTC, St. Johns, 1989, p. 44–53.
- [56] Stutz B, Reboud JL. Two-phase flow structure of sheet cavitation. Phys Fluids 1997;9(12):3678–86.
- [57] Chen Y, Heister SD. A numerical treatment for attached cavitation. J Fluids Eng 1994;116:613–8.
- [58] Deshpande M, Feng J, Merkle CL. Numerical modeling of the thermodynamic effects of cavitation. J Fluids Eng 1997;119:420–7.
- [59] Delannoy Y, Kueny JL. Cavity flow predictions based on the Euler equations. ASME Cavitation and Multi-Phase Flow Forum, 1990;109:153–8.
- [60] Chen Y, Heister SD. Modeling hydrodynamic nonequilibrium in cavitating flows. J Fluids Eng 1996;118: 172–8.
- [61] Ventikos Y, Tzabiras G. A numerical method for the simulation of steady and unsteady cavitating flows. Comput Fluids 2000;29:63–88.
- [62] Edwards JR, Franklin RK, Liou MS. Low-diffusion flux-splitting methods for real fluid flows with phase transitions. AIAA J 2000;38(9):1624–33.
- [63] Rayleigh L. On the pressure developed in a liquid during the collapse of a spherical cavity. Philos Mag 1917;34:94–8.
- [64] Plesset MS. The dynamics of cavitation bubbles. Trans ASME J Appl Mech 1949;16:228–31.
- [65] Singhal AK, Vaidya N, Leonard AD. Multi-dimensional simulation of cavitating flows using a PDF model for phase change. ASME Paper FEDSM97-3272, The 1997 ASME Fluids Engineering Division Summer Meeting, 1997.
- [66] Merkle CL, Feng J, Buelow PEO. Computational modeling of the dynamics of sheet cavitation. Third International Symposium on Cavitation, Grenoble, France, 1998.
- [67] Kunz RF, Chyczewski TS, Boger DA, Stinebring DR, Gibeling HJ. Multi-phase CFD analysis of natural and ventilated cavitation about submerged bodies. ASME Paper FEDSM99-7364, Proceedings of the Third ASME/JSME Joints Fluids Engineering Conference, 1999.
- [68] Kunz RF, Boger DA, Stinebring DR, Chyczewski TS, Lindau JW, Gibeling HJ, Venkateswaran S, Govindan TR. A preconditioned Navier–Stokes method for two-phase flows with application to cavitation prediction. Comput Fluids 2000;29:849–75.

- [69] Ahuja V, Cavallo PA, Hosangadi, A. Multi-phase flow modeling on adaptive unstructured meshes. AIAA Fluids 2000 and Exhibit, Paper No. AIAA-2000-2662, June 19–22, Denver, Colorado, 2000.
- [70] Venkateswaran S, Lindau JW, Kunz RF, Merkle CL. Preconditioning algorithms for the computation of multi-phase mixture flows. AIAA 39th Aerospace Sciences Meeting and Exhibit, Paper No. 2001-0125, 2001.
- [71] Senocak I, Shyy W. A pressure-based method for turbulent cavitating flow computations. 31st AIAA Fluid Dynamics Conference and Exhibit, AIAA 2001-2907 (<http://www.aero.ufl.edu/cfd/>). J Comput Phys (submitted for publication).
- [72] Senocak I, Shyy W. Numerical simulation of turbulent flows with sheet cavitation. CAV2001, Proceedings of the Forth International Symposium on Cavitation, Paper No. CAV2001A7.002 2001, California Institute of Technology, Pasadena, CA, USA. June 20–23, 2001 (<http://cav2001.library.caltech.edu/>).
- [73] Patankar SV. Numerical heat transfer, fluid flow. Washington DC: Hemisphere, 1980.
- [74] Vandoormaal JP, Raithby GD. Enhancements of the SIMPLE method for predicting incompressible fluid flows. Numer Heat Transf 1984;7:147–63.
- [75] Shyy W. Computational modeling for fluid flow, interfacial transport. Amsterdam, The Netherlands: Elsevier, 1994 (revised printing 1997).
- [76] Shyy W, Correa SM, Braaten ME. Computation of flow in a gas turbine combustor. Combust Sci Tech 1988;58:97–117.
- [77] Carey VP. Liquid-vapor phase-change phenomena. Washington, DC: Hemisphere, 1992.
- [78] Colonius T, d'Auria F, Brennen CE. Acoustic saturation in bubbly cavitating flow adjacent to an oscillating wall. Phys Fluids 2000;12(11):2752–61.
- [79] Joseph DD. Cavitation in a flowing liquid. Phys Rev E 1995;51(3):1649.
- [80] Jones WP, Launder BE. The prediction of laminarization with a two-equation model of turbulence. Int J Heat Mass Transfer 1972;15:301–14.
- [81] Launder BE, Spalding DB. The numerical computation of turbulent flows. Comput Math Appl Mech Eng 1974;3:269–89.
- [82] Shyy W, Thakur SS, Ouyang H, Liu J, Blosch E. Computational techniques for complex transport phenomena. New York: Cambridge University Press, 1997.
- [83] Lien FS, Leschziner MA. Second-moment closure for three-dimensional turbulent flow around and within complex geometries. Comput Fluids 1996;25:237–62.
- [84] Shih T, Liou WW, Shabbir A, Yang Z, Zhu J. A new  $k-\epsilon$  eddy viscosity model for high Reynolds number turbulent flows. Comput Fluids 1995;24:227–38.
- [85] Speziale CG. A review of Reynolds stress models for turbulent shear flows, 1995, NASA CR-195054.
- [86] Shyy W, Krishnamurthy V. Compressibility effect in modeling complex turbulent flows. Prog Aerosp Sci 1997;33:587–645.
- [87] Craft TJ, Launder BE. A Reynolds stress closure designed for complex geometries. Int J Heat Fluid Flow 1996;17:245–54.
- [88] Leschziner M. Turbulence modeling for separated flows with anisotropy-resolving closures. Philos Trans R Soc London A 2000;358:3247–77.
- [89] Thakur S, Shyy W. Reynolds stress models for flows in complex geometries: review and application, AIAA 30th Fluid Dynamics Conference, 1999; Paper No. 99-3782.
- [90] Gatski TB, Jongen T. Nonlinear eddy viscosity and algebraic stress models for solving complex turbulent flows. Prog Aerosp Sci 2000;36:655–82.
- [91] Kenjeres S, Hanjalic K. Transient analysis of Rayleigh-Benard convection with a RANS model. Int J Heat Fluid Flow, 1999;20:329–40.
- [92] Jimenez J, Moser RD. Large-eddy simulations: where are we and what can we expect? AIAA J, 2000;38:605–12.
- [93] Shyy W, Braaten ME. Adaptive grid computation for inviscid compressible flows using a pressure correction method. Proceedings of the AIAA/ASME/SIAM/APS First National Fluid Dynamics Congress, AIAA-CP 888, 1988. p. 112–120.
- [94] Karki KC, Patankar SV. Pressure based calculation procedure for viscous flows at all speeds in arbitrary configurations. AIAA J 1989;27(9):1167–74.
- [95] Ferziger JH, Peric M. Computational methods for fluid dynamics, 2nd edition. Berlin, Germany: Springer Verlag, 1999.
- [96] Lindau JW, Kunz RF, Venkateswaran S, Boger DA. Application of preconditioned, multiple-species, Navier–Stokes models to cavitating flows. CAV2001, Proceedings of 4th International Symposium on Cavitation, Paper No. CAV2001B4.005, California Institute of Technology, Pasadena, CA USA. June 20–23, 2001.
- [97] Taylor LK, Arabshahi A, Whitfield DL. Unsteady three-dimensional incompressible Navier–Stokes computations for a prolate spheroid undergoing time-dependent maneuvers. AIAA Paper 95-0313, 1995.
- [98] Whitfield DL, Taylor LK. Numerical solution of the two-dimensional time-dependent incompressible Euler equations. Mississippi State University CFD Laboratory Report MSSU-EIRS-ERC-93-14, 1994.
- [99] Chorin AJ. A numerical method for solving incompressible viscous flow problems. J Comput Phys 1967;2:12–26.
- [100] Shyy W, Liu J, Ouyang H. Multi-resolution computations for fluid flow and heat/mass transfer. In: Minkowycz WJ, Sparrow EM, editors. Advances in Numerical Heat Transfer, Vol. 1. Washington, DC: Taylor & Francis, 1997. p. 137–69.
- [101] Shyy W, Udaykumar HS, Rao MM, Smith RW. Computational fluid dynamics with moving boundaries. Washington, DC: Hemisphere, 1996.
- [102] Rouse H, McNown JS. Cavitation and pressure distribution, head forms at zero angle of yaw. Studies in Engineering, Bulletin 32, State University of Iowa, Iowa, 1948.